The Astrophysical Journal, 861:100 (15pp), 2018 July 10 https://doi.org/10.3847/1538-4357/aac6ba
© 2018. The American Astronomical Society. All rights reserved.

An ALMA Survey of the SCUBA-2 Cosmology Legacy Survey UKIDSS/UDS Field: Identifying Candidate $z \sim 4.5$ [C II] Emitters

E. A. Cooke[1], Ian Smail[1], A. M. Swinbank[1], S. M. Stach[1], Fang Xia An[1,2], B. Gullberg[1], O. Almaini[3], C. J. Simpson[4], J. L. Wardlow[1], A. W. Blain[5], S. C. Chapman[6], Chian-Chou Chen[7], C. J. Conselice[3], K. E. K. Coppin[8], D. Farrah[9,10], D. T. Maltby[3], M. J. Michałowski[11], D. Scott[12], J. M. Simpson[13], A. P. Thomson[14], and P. van der Werf[15]

[1] Centre for Extragalactic Astronomy, Department of Physics, Durham University, Durham, DH1 3LE, UK; elizabeth.a.cooke@durham.ac.uk
[2] Purple Mountain Observatory, China Academy of Sciences, 2 West Beijing Road, Nanjing 210008, People's Republic of China
[3] School of Physics and Astronomy, University of Nottingham, University Park, Nottingham NG7 2RD, UK
[4] Gemini Observatory, Northern Operations Center, 670 N. A'ohōkū Place, Hilo, HI 96720, USA
[5] Physics & Astronomy, University of Leicester, 1 University Road, Leicester LE1 7RH, UK
[6] Department of Physics and Atmospheric Science, Dalhousie University, Halifax, NS B3H 4R2, Canada
[7] European Southern Observatory, Karl Schwarzschild Strasse 2, Garching, Germany
[8] Centre for Astrophysics Research, School of Physics, Astronomy and Mathematics, University of Hertfordshire, College Lane, Hatfield AL10 9AB, UK
[9] University of Hawaii, 2505 Correa Road, Honolulu, HI 96822, USA
[10] Department of Physics, Virginia Tech, Blacksburg, VA 24061, USA
[11] Astronomical Observatory Institute, Faculty of Physics, Adam Mickiewicz University, ul. Słoneczna 36, 60-286 Poznań, Poland
[12] Department of Physics & Astronomy, University of British Columbia, 6224 Agricultural Road, Vancouver, BC V6T 1Z1, Canada
[13] Academia Sinica Institute of Astronomy and Astrophysics, No. 1, Sec. 4, Roosevelt Road, Taipei 10617, Taiwan
[14] Jodrell Bank Centre for Astrophysics, School of Physics and Astronomy, The University of Manchester, Oxford Road, Manchester, M13 9PL, UK
[15] Leiden Observatory, Leiden University, P.O. Box 9513, NL-2300 RA Leiden, The Netherlands
Received 2018 February 6; revised 2018 May 9; accepted 2018 May 12; published 2018 July 10

Abstract

We report the results of a search for serendipitous [C II] 157.74 μm emitters at $z \simeq 4.4$–4.7 using the Atacama Large Millimeter/submillimeter Array (ALMA). The search exploits the AS2UDS continuum survey, which covers $\sim$50 arcmin^2 of the sky toward 695 luminous ($S_{870} \gtrsim 1$ mJy) submillimeter galaxies (SMGs), selected from the SCUBA-2 Cosmology Legacy Survey 0.96 deg^2 Ultra Deep Survey (UDS) field. We detect 10 candidate line emitters, with an expected false detection rate of 10%. All of these line emitters correspond to 870 μm continuum-detected sources in AS2UDS. The emission lines in two emitters appear to be high-J CO, but the remainder have multi-wavelength properties consistent with [C II] from $z \simeq 4.5$ galaxies. Using our sample, we place a lower limit of $>5 \times 10^{-6}$ Mpc^{-3} on the space density of luminous ($L_{\rm IR} \simeq 10^{13}\,L_\odot$) SMGs at $z = 4.40$–4.66, suggesting $\geqslant$7% of SMGs with $S_{870\,\mu{\rm m}} \gtrsim 1$ mJy lie at $4 < z < 5$. From stacking the high-resolution ($\sim$0.″15 full-width half maximum) ALMA 870 μm imaging, we show that the [C II] line emission is more extended than the continuum dust emission, with an average effective radius for the [C II] of $r_{\rm e} = 1.7^{+0.1}_{-0.2}$ kpc, compared to $r_{\rm e} = 1.0 \pm 0.1$ kpc for the continuum (rest-frame 160 μm). By fitting the far-infrared photometry for these galaxies from 100 to 870 μm, we show that SMGs at $z \sim 4.5$ have a median dust temperature of $T_{\rm d} = 55 \pm 4$ K. This is systematically warmer than 870 μm selected SMGs at $z \simeq 2$, which typically have temperatures around 35 K. These $z \simeq 4.5$ SMGs display a steeper trend in the luminosity-temperature plane than $z \leqslant 2$ SMGs. We discuss the implications of this result in terms of the selection biases of high-redshift starbursts in far-infrared/submillimeter surveys.

Key words: galaxies: high-redshift – submillimeter: galaxies

1. Introduction

Despite their high individual luminosities, ultra-luminous infrared galaxies (ULIRGs; $L_{\rm IR} > 10^{12}\,L_\odot$) contribute less than 1% of the local star formation rate density (e.g., Magnelli et al. 2011; Casey et al. 2012). The situation at higher redshifts, however, appears to be very different. Measurements of the redshift distribution of high-redshift ULIRGs, including those detected at submillimeter wavelengths (so-called "submillimeter galaxies," SMGs; Smail et al. 1997) show a rapid rise ($\sim$1000-fold increase) in their volume density to a peak at $z \simeq 2.5$ and a decline at high redshifts (e.g., Aretxaga et al. 2003; Chapman et al. 2005; Wardlow et al. 2011; Casey et al. 2012; Yun et al. 2012; Simpson et al. 2014, 2017a; Michałowski et al. 2017). At $z \gtrsim 1$ SMGs may contribute up to 50% of the star formation rate density (e.g., Peacock et al. 2000; Chapman et al. 2005; Barger et al. 2012; Casey et al. 2014; Swinbank et al. 2014; Zavala et al. 2017). SMGs at higher redshifts ($z \gtrsim 3$) may also hold the key to explaining the populations of $z \sim 2$–3 compact, quiescent galaxies now being detected (e.g., Toft et al. 2014; Hodge et al. 2016; Simpson et al. 2017b). The high stellar masses and apparent old ages of these galaxies suggest that they formed in rapid, intense bursts of star formation at $z > 3$ (e.g., Glazebrook et al. 2017; Simpson et al. 2017b). Such starbursts may be linked to high-redshift SMGs (e.g., Ikarashi et al. 2015), meaning these galaxies are an essential element in models of massive galaxy formation.

High-redshift ($z \gtrsim 3$) SMGs therefore appear to play a potentially significant role in galaxy evolution; however, their dusty nature and high redshift mean that measuring their spectroscopic redshifts—needed to constrain many of their basic properties—is extremely challenging using ground-based optical/near-infrared spectroscopy. As a result, the redshift distribution of SMGs is increasingly incomplete at $z \gtrsim 3$ (e.g., Danielson et al. 2017).

Some progress can be made in identifying $z > 3$ SMGs using far-infrared photometry to measure their infrared spectral

energy distribution (SED, e.g., to identify "500 μm risers"; Dowell et al. 2014). However, the degeneracy in the SED shape between dust temperature and redshift make the derived redshifts highly uncertain (e.g., Blain 1999; Béthermin et al. 2015; Schreiber et al. 2018).

For the subset of optical/near-infrared bright SMGs where reliable photometric redshifts can be measured, recent studies have suggested that $z \gtrsim 4$ SMGs are characterized by far-infrared SEDs that have warmer dust temperatures than SMGs at $z \simeq 2$ ($\sim$40–50 K compared to $\sim$35 K; e.g., Swinbank et al. 2014; Schreiber et al. 2017). Although there are potentially biases in the derived characteristic temperatures due to selection effects, the higher dust temperatures inferred at $z \simeq 4$ may also be driven by physical differences in galaxy properties compared to SMGs at $z \simeq 2$, for example, by reflecting the size of the dust regions or the star formation rate of the galaxy. Alternatively, higher star formation efficiencies in $z \gtrsim 4$ SMGs (which may have shorter dynamical times than SMGs at $z \simeq 2$) may result in the warmer dust temperatures. However, these results rely on uncertain photometric redshifts and hence to reliably constrain any evolution in characteristic dust temperatures with redshift, precise spectroscopic redshifts for $z > 3$ galaxies are required.

(Sub)millimeter spectroscopy provides one of the most reliable means to derive redshifts for distant SMGs, especially at $z \gtrsim 3$ where the multi-wavelength counterparts are faint or undetected in the optical/near-infrared. With the advent of the Atacama Large Millimeter/submillimeter Array (ALMA) it is now possible to obtain high-resolution imaging and spectroscopy in submillimeter wavebands. This allows us to both efficiently target single-dish submillimeter sources and precisely locate the counterpart of the SMG, and also to search for emission lines in the far-infrared to measure spectroscopic redshifts.

The $^2P_{3/2} \rightarrow {}^2P_{1/2}$ fine structure line of C^+ at 157.74 μm (hereafter [C II]) is one of the primary routes by which interstellar gas can cool and consequently is typically the strongest emission line in the far-infrared spectra of star-forming galaxies. [C II] emission can account for up to 2% of the total bolometric luminosity in a galaxy (e.g., Brauher et al. 2008), although with one dex of scatter at a fixed far-infrared luminosity (e.g., Díaz-Santos et al. 2013). The scatter arises due to the complex mix of processes that generate [C II] emission. For example, [C II] emission can originate both in photodissociation regions around star-forming regions and also from atomic and ionized gas (e.g., Dalgarno & McCray 1972; Madden et al. 1997; Pineda et al. 2013). [C II] could thus provide information about the volume and extent of the cold gas reservoir and star formation in galaxies. In particular for star-forming galaxies, the photodissociation regions can dominate the [C II] emission so several studies have shown the [C II] emission line correlates with the star formation rate (e.g., Stacey et al. 1991; Graciá-Carpio et al. 2011; De Looze et al. 2014).

To date, one of the largest samples of interferometrically identified SMGs available is the ALMA-LABOCA Extended *Chandra* Deep Field-South Survey (ALESS; Hodge et al. 2013), which identified 99 SMGs, 21 of which are likely to lie at $z > 4$ given their multi-wavelength properties (Simpson et al. 2014). At $z \sim 4$–5 [C II] is redshifted to $\sim$870 μm. In two of the ALESS sources [C II] was serendipitously detected in the ALMA Band 7 observations at a redshift of $z = 4.42$–4.44 (Swinbank et al. 2012), placing weak constraints on the properties of these galaxies and the [C II] luminosity function at this redshift. However, with only two sources, a larger spectroscopic sample is clearly required in order to improve our understanding of the properties of $z \geqslant 4$ SMGs.

To increase the sample size of high-redshift SMGs, we have undertaken the ALMA-SCUBA-2 survey of the Ultra Deep Survey (UDS) field (AS2UDS): an ALMA Band 7 survey of all 716 submillimeter sources detected in the UKIDSS UDS field by SCUBA-2 on the James Clerk Maxwell Telescope (JCMT; Geach et al. 2017). This survey has precisely located 695 SMGs (S. M. Stach et al. 2018, in preparation). Here, we examine the ALMA datacubes to search for serendipitous emission lines. The frequency coverage of our data is 336–340 and 348–352 GHz, corresponding to $z = 4.40$–4.46 and $z = 4.60$–4.66 for [C II]. We aim to spectroscopically confirm [C II] emission line sources at $z \simeq 4.5$ and thus determine their basic properties such as infrared luminosity and dust temperature, as well as measure the number density of SMGs at $z > 4$.

The paper is laid out as follows. In Section 2 we outline the observations and data reduction. Section 3 presents our results and discussion. Our conclusions are given in Section 4. Throughout we use AB magnitudes and assume a ΛCDM cosmology with $\Omega_M = 0.3$, $\Omega_\Lambda = 0.7$, and $H_0 = 70\,\mathrm{km\,s^{-1}\,Mpc^{-1}}$.

2. Observations, Data Reduction, and Analysis

2.1. ALMA Data

The UDS 0.96 degree^2 field was observed at 850 μm with SCUBA-2 as part of the Cosmology Legacy Survey (Geach et al. 2017) to a depth of $\sigma_{850} \simeq 0.9$ mJy beam^{-1}, detecting 716 submillimeter sources above 4σ, $S_{850} \simeq 3.6$ mJy. We observed all 716 of these submillimeter sources with ALMA at 870 μm in Band 7 to pinpoint the galaxies responsible for the submillimeter emission. The data were taken in the period 2013 November to 2017 May (Cycles 1, 3, and 4) with a dual polarization setup. The full data reduction and catalog will be presented in S. M. Stach et al. (2018, in preparation). In brief, our observations cover a total bandwidth of 7.5 GHz split into two sidebands: 336–340 GHz and 348–352 GHz. The synthesized beam of our observations is 0.15–0.3 arcsec FWHM, adopting natural weighting. The primary beam of ALMA is $\sim$18 arcsec FWHM, which covers the SCUBA-2 beam (FWHM $\sim$ 14.5 arcsec). This coverage, combined with the higher resolution and greater depth of the ALMA observations, means that we expect to detect the sources responsible for the original SCUBA-2 detections in the ALMA continuum data.

Each pointing was centered on the SCUBA-2 catalog position and observed for a total of $\sim$40 s. A subset of 120 of the pointings were observed in both Cycles 3 and 4 and thus have a longer total integration time (typically 80–90 s). All data were processed using the Common Astronomy Software Application (CASA; McMullin et al. 2007). We construct cleaned, tapered continuum maps and dirty, tapered datacubes. For more reliable line detections, we image the cubes without applying any cleaning to deconvolve the beam. The final cleaned, 0.″5 FWHM-tapered continuum maps have average depths of $\sigma_{870\,\mu\mathrm{m}} = 0.25$, 0.34, and 0.23 mJy beam^{-1} for Cycle 1, 3, and 4 data, respectively. S. M. Stach et al. (2018, in preparation) will present an analysis of the data, catalog construction, and multi-wavelength properties.

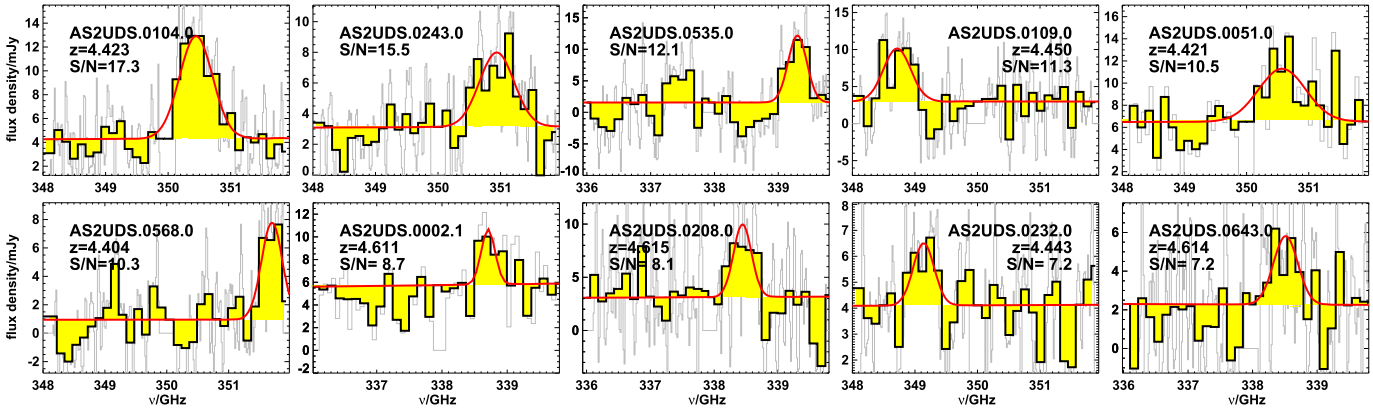

Figure 1. Emission lines detected in the AS2UDS Band 7 datacubes, ranked by their integrated S/N. These are labeled with the SMG ID, the S/N and the corresponding redshift if the line is [C II] 157.74 μm. We find 10 line emitters with integrated S/N ranging from S/N = 7.2–17.3 in the 695 SMGs with $S_{870\ \mu\mathrm{m}} \gtrsim 1$ mJy. Fluxes shown are not primary beam-corrected (typically a correction of <10%) and are measured at the position of peak flux within the 0.5 arcsec tapered dirty cubes. The gray lines show the unbinned data. The black histogram shows the data binned to 100 km s^{-1}. The red lines show the Gaussian fit to the detected emission line and continuum level. We note that AS2UDS.0243.0 and AS2UDS.0535.0 have photometric properties that suggest the line we detect is CO(8–7) or CO(5–4), respectively, corresponding to $z_{\mathrm{CO}} < 2$. Further observations are needed to confirm the nature of these emission lines.

ALMA continuum sources were identified in the continuum maps as submillimeter sources with a signal-to-noise ratio (S/N) S/N $\geqslant$ 4.3 within a 0.5 arcsec diameter aperture, calculated from the aperture-integrated flux and the noise measured in randomly placed apertures for each map. This S/N limit provides a 2% false-positive rate, as determined by inverting the maps. In total we selected 695 ALMA continuum-detected SMGs brighter than $S_{870} \gtrsim 1$ mJy, which will be discussed in S. M. Stach et al. (2018, in preparation).

To search for emission lines, we use the dirty datacubes, which were constructed at raw spectral resolution ($\sim$13.5 km s^{-1}) and tapered to 0.″5 FWHM resolution to match the continuum maps by applying a $\sim$400 kλ Gaussian *uv* taper. These cubes were first continuum-subtracted by subtracting a linear fit to the continuum in the spectrum of each pixel.[16] These continuum-subtracted cubes were also used to calculate [C II] emission sizes in Section 3.4.

To search for emission lines in the datacubes, we velocity-binned the 0.″5 tapered, continuum-subtracted cubes to 50, 100, and 200 km s^{-1} channels and then extracted the spectra at the position of each AS2UDS continuum-selected SMG. We search each of these spectra for peaks with S/N $\geqslant$ 2. These were then refit in the 50 km s^{-1} channel spectrum using a Gaussian profile and the integrated S/N calculated within the FWHM of the line.

Given the non-Gaussian nature of the noise in the ALMA datacubes, to determine the purity of the sample and hence an acceptable S/N threshold for our detections, we calculate an empirical false-positive rate by applying the same procedure to the inverted, velocity-binned, continuum-subtracted cubes at the AS2UDS source positions. This false-positive rate is dependent on the velocity binning of the spectra. We require a threshold for selection that produces a false detection rate of 10%.

For a false-positive rate of ten percent in our final sample, we take an integrated S/N cut that varies depending upon the velocity binning with S/N = 8.0 for 50 km s^{-1} channels, S/N = 7.5 for 100 km s^{-1} channels, and S/N = 7.0 for 200 km s^{-1} channels. We detect significant emission lines in 10 SMGs above these limits. We plot all 10 line emitters in Figure 1 and list their properties in Tables 1 and 2.

To ensure we identify all bright line emitters within the ALMA pointings, we run two additional line searches. First, two of the SMGs where we have identified an emission line lie in ALMA maps that contain a second SMG. In these cases we extract the spectra of this second SMG and search for (lower-significance) emission lines at similar frequencies to the detected emission line. In one of these SMGs (AS2UDS.0109.1) we found a tentative S/N = 5.3 emission line corresponding to the same redshift as the detected emission line source (AS2UDS.0109.0). We include this SMG as a "supplementary" source[17] and the spectra and optical/near-infrared thumbnails are shown in Appendix A. If confirmed, this secondary source would be located 70 kpc in projection and 50 km s^{-1} offset in redshift from the primary source.

Second, we also searched the 695 ALMA cubes for emission line sources lacking continuum counterparts. In each continuum-subtracted cube we step through the cube, collapsing in velocity bins of 100 km s^{-1} ($\sim$7 resolution elements), the centers of which are shifted by 50 km s^{-1} between slices.[18] In each collapsed 100 km s^{-1} slice we search in the narrowband image for peaks above 2σ within the ALMA primary beam. For any peak detected we extract and fit a Gaussian profile to the full spectrum and measure the integrated S/N of the line. We perform the same search on the inverted cubes to calculate a false-positive rate. Using this method we find no additional emission line sources within the ALMA pointings above a false-positive rate of 50%, corresponding to a line flux limit of $Sdv \gtrsim 1$ Jy km s^{-1}.

2.2. Multi-wavelength Data

The UDS has photometric coverage spanning the optical, near-, mid-, and far-infrared, out to radio wavelengths.

The UKIRT Infrared Deep Sky Survey (UKIDSS; Lawrence et al. 2007) UDS data release 11 (DR11) photometric catalog (O. Almaini et al., in preparation) is based on a deep,

[16] Second-order polynomial and constant fits were also tested, but the linear fit produced a good fit to the data without over-fitting.

[17] The false-positive rate at this significance and line width is $\sim$50%, so this source requires further observations in order to confirm it.

[18] We also tested channels of 50 and 200 km s^{-1} with step sizes that were half the channel sizes, but no additional significant emission lines were detected.

Table 1
Table of Emission Line Candidates and Line Properties

Source ID[a]	R.A. (J2000)	Decl. (J2000)	S_{870}[b] (mJy)	ν_{obs}[c] (GHz)	$z_{[C\,II]}$[d]	FWHM$_{[C\,II]}$[e] (km s^{-1})	$S\,dv_{[C\,II]}$ (Jy km s^{-1})	S/N[f]
AS2UDS.0002.1	02:18:24.24	−05:22:56.9	7.4 ± 0.5	338.707	4.611 ± 0.009	220 ± 50	1.3 ± 0.3	8.7
AS2UDS.0051.0	02:19:24.84	−05:09:20.8	6.3 ± 0.4	350.571	4.421 ± 0.006	770 ± 80	4.0 ± 0.4	10.5
AS2UDS.0104.0	02:16:22.73	−05:24:53.3	5.6 ± 0.3	350.447	4.423 ± 0.007	530 ± 60	4.9 ± 0.6	17.3
AS2UDS.0109.0	02:16:18.37	−05:22:20.1	5.5 ± 0.7	348.715	4.450 ± 0.007	440 ± 40	4.5 ± 0.4	11.3
AS2UDS.0208.0	02:19:02.88	−04:59:41.5	4.0 ± 0.7	338.445	4.615 ± 0.009	290 ± 40	2.2 ± 0.3	8.1
AS2UDS.0232.0	02:15:54.66	−04:57:25.6	4.6 ± 0.3	349.140	4.443 ± 0.008	340 ± 90	0.9 ± 0.2	7.2
AS2UDS.0243.0[g]	02:16:17.91	−05:07:18.9	4.3 ± 0.3	350.939	⋯	560 ± 70	3.2 ± 0.4	15.5
AS2UDS.0535.0[h]	02:18:13.30	−05:30:29.1	2.4 ± 0.5	339.301	⋯	310 ± 20	3.6 ± 0.2	12.1
AS2UDS.0568.0	02:18:40.02	−05:20:05.6	1.2 ± 0.3	351.701	4.404 ± 0.009	340 ± 60	2.8 ± 0.5	10.3
AS2UDS.0643.0	02:16:51.31	−05:15:37.2	2.2 ± 0.4	338.512	4.614 ± 0.007	390 ± 110	1.5 ± 0.4	7.2
Median values[i]	⋯	⋯	4.4 ± 0.6	⋯	4.45 ± 0.03	370 ± 50	3.0 ± 0.1	10.4 ± 1.1
Supplementary catalog[j]								
AS2UDS.0109.1	02:16:19.04	−05:22:23.2	2.6 ± 0.6	348.653	4.45 ± 0.01	270 ± 40	1.6 ± 0.2	5.3

Notes.
[a] Source IDs, coordinates, and 870 μm flux densities come from the full AS2UDS catalog presented in S. M. Stach et al. (2018, in preparation).
[b] The continuum flux densities are primary beam-corrected and were measured in 1 arcsec diameter apertures in the 0.5 arcsec FWHM-tapered maps.
[c] Observed frequencies correspond to the peak of the detected emission line.
[d] Redshifts are derived assuming the detected emission line is [C II].
[e] The FWHM and flux density (and their respective uncertainties) of each line are measured from a Gaussian fit to the emission line.
[f] S/N measurements come from integrating the spectrum across the line between ν_{obs} −0.5 × FWHM and ν_{obs} + 0.5 × FWHM.
[g] AS2UDS.0243.0 has optical, near-infrared, and radio properties that may indicate the line we detect is CO(8–7), corresponding to $z_{CO} = 1.63 \pm 0.01$.
[h] AS2UDS.0535.0 has optical and near-infrared properties that may indicate the line we detect is CO(5–4), corresponding to $z_{CO} = 0.70 \pm 0.01$.
[i] Uncertainties on median values are the standard error.
[j] Supplementary sources are those within the same ALMA map as a detected line emitter (but not detected above our S/N threshold), which appear to have a low-significance emission line at a similar frequency to their detected companion.

K-band-selected catalog down to a 3σ depth of $K = 25.9$ mag, with additional imaging in *U*, *B*, *V*, *R*, *I*, *J*, *H*, *K*, and *Spitzer*/IRAC.

To derive the photometric properties of our sample, we match our sources to the UDS DR11 using a search radius of 0.6 arcsec, giving a false-match rate of 3.5% (An et al. 2018). Three-color 5″ × 5″ thumbnails of the 10 candidate line emitters are shown in Figure 2. This figure also shows a zoomed-in 3″ × 3″ optical/infrared image of each source, with the ALMA continuum contours overlaid. We use these thumbnails to assess the multi-wavelength properties of the line emitters, in particular to determine if the optical/infrared photometry is contaminated by nearby galaxies.

The UDS20 project (V. Arumugam et al., in preparation) imaged the UDS at 1.4 GHz using the Very Large Array. The total area coverage is ∼1.3 degrees^2, with the ∼160 hr integration resulting in an rms noise of ∼6 μJy beam^{-1} across the full field. A full description of the radio data will be presented in V. Arumugam et al. (in preparation).

The UDS also has coverage with the *Herschel Space Observatory* Photoconductor Array Camera and Spectrometer (PACS; Poglitsch et al. 2010) and Spectral and Photometric Imaging REceiver (SPIRE; Griffin et al. 2010) at 100, 160, 250, 350, and 500 μm. The resolution of the far-infrared *Herschel* wavebands (15–35 arcsec) requires the data to be deblended in order to obtain the photometry of our SMGs.

For the deblending we follow the method described in Swinbank et al. (2014).[19] The deblending uses a combination of the ALMA-detected SMGs and *Spitzer*/MIPS 24 μm and UDS20 radio sources as positional priors for the deblending of the low-resolution SPIRE maps. To deblend the SPIRE maps we use a Monte Carlo algorithm that fits the observed flux distribution with beam-sized components at the position of each source in the prior catalog. This is then iterated toward solutions that yield the range of possible fluxes associated with each source. To ensure that we do not "over deblend," the method is first applied at 250 μm. Any sources in the prior catalog that are detected at 250 μm above 2σ are then used as the prior list for the 350 μm deblending, and similarly those detected above >2σ at 350 μm are then used in the 500 μm deblending. There are averages of 2.4, 2.0 and 1.9 priors within the FWHM of the beam centered at the ALMA position (i.e., 15 arcsec, 25 arcsec and 35 arcsec at 250 μm, 350 μm, and 500 μm respectively). By attempting to recover false positives injected into the maps we derive 3σ detection limits of 7.0, 8.0, and 10.6 mJy at 250, 350, and 500 μm, respectively (see Swinbank et al. 2014 for details). The ALMA sources are included at all wavelengths so as not to bias their SEDs. We discuss the *Herschel* fluxes and far-infrared SED fits in more detail in Section 3.3.

3. Results and Discussion

We identify emission lines in 10 AS2UDS continuum sources: three with integrated S/N > 7.0 in the 200 km s^{-1} channel spectra, six with integrated S/N > 7.5 at 100 km s^{-1}, and one with integrated S/N > 8.0 at 50 km s^{-1}. Figure 1 shows the spectra of these sources binned to 100 km s^{-1} channels (we also show the data at the native resolution). We provide the source redshifts and line properties in Table 1. The line flux densities are calculated from the Gaussian profile fit to each line.

[19] The deblended catalogs for the fields are available from http://astro.dur.ac.uk/~ams/HSOdeblend.

Table 2
Photometric Properties of Line Emitters

Source ID	V[a] (mag)	K (mag)	4.5 μm (mag)	S_{250} (mJy)	S_{350} (mJy)	S_{500} (mJy)	$S_{1.4\ \mathrm{GHz}}$ (μJy)	z_{phot}	Potential Contamination?[b]
AS2UDS.0002.1	*26.85 ± 0.25*	*23.97 ± 0.06*	*22.76 ± 0.02*	*31 ± 4*	*35 ± 5*	*43 ± 7*	*<80*	⋯	Y: lens?
AS2UDS.0051.0	>27.47	23.32 ± 0.04	21.93 ± 0.02	<9	<11	<12	<80	⋯	N
AS2UDS.0104.0	⋯	24.03 ± 0.06	23.50 ± 0.08	<9	<11	<12	<80	⋯	N
AS2UDS.0109.0	⋯	22.88 ± 0.03	22.56 ± 0.07	<9	11 ± 3	<14	<80	⋯	N
AS2UDS.0208.0	*26.11 ± 0.10*	*22.94 ± 0.01*	*21.28 ± 0.01*	*<9*	*<12*	*<12*	*<80*	⋯	Y: lens?
AS2UDS.0232.0	⋯	⋯	22.42 ± 0.01	24 ± 4	20 ± 4	<12	<80	⋯	N
AS2UDS.0243.0	*23.21 ± 0.01*	*20.68 ± 0.01*	*20.17 ± 0.01*	*32 ± 5*	*<17*	*<17*	*1220 ± 30*	$1.58^{+0.05}_{-0.05}$	Y: low-z CO?
AS2UDS.0535.0	*25.95 ± 0.09*	*23.44 ± 0.04*	*22.98 ± 0.07*	*12 ± 3*	*13 ± 3*	*<15*	*<80*	$0.80^{+0.03}_{-0.03}$[c]	Y: low-z CO?
AS2UDS.0568.0	>27.8	24.36 ± 0.06	23.39 ± 0.05	<18	<16	<12	<80	3.5 ± 1.0	N
AS2UDS.0643.0	*>27.8*	*24.30 ± 0.03*	*21.80 ± 0.01*	*14 ± 3*	*11 ± 3*	*<13*	*105 ± 18*	$4.4^{+0.6}_{-1.1}$	Y: lens?
Median values[d]	26.11 ± 0.33	23.44 ± 0.13	22.49 ± 0.10	24 ± 2	13 ± 2	<13	<80	⋯	⋯
Supplementary catalog									
AS2UDS.0109.1	⋯	24.02 ± 0.07	23.28 ± 0.13	<9	<11	<12	<80	⋯	N

Notes.
[a] Photometry and redshifts are taken from the UDS DR11 catalog (O. Almaini et al., in preparation) and the UDS20 radio catalog (V. Arumugam et al., in preparation). Ellipses indicate no photometric coverage.
[b] Italics indicates that the SMG has a nearby source that may contaminate the photometry. Some or all of these sources may also be lensed (final column); see Section 3.1.
[c] AS2UDS.0535.0 has a secondary peak in its photometric redshift distribution at $z = 4.63$ (see Appendix B).
[d] Uncertainties on median values are the standard errors.

The number of line emitters we identify from the parent sample of 695 SMGs is consistent with the expectation from the ALESS survey, where two emission line sources were identified from a sample of 99 SMGs (Swinbank et al. 2012).

3.1. Alternative Emission Lines

Before we discuss the properties of our line-emitter galaxies, we first discuss the identification of the emission lines. Within the ISM of dusty star-forming galaxies, the brightest emission line in the rest-frame far-infrared is expected to be [C II] λ157 μm. At observed frame 870 μm this would correspond to $z \sim 4.5$. [C II] dominates the cooling of the ISM for temperatures $T < 100$ K, and as noted earlier, may contribute up to two percent of the bolometric luminosity (e.g., Smail et al. 2011). However, there may be contamination from other emission lines in our sample such as [N II] λ122 μm at $z \sim 6.1$, [O I] λ145 μm at $z \sim 4.9$, [N II] λ205 μm at $z \sim 3.1$, or high-J ^{12}CO at $z = 0.3$–2.7 ($4 < J_{\mathrm{up}} < 11$). In typical sources the [C II] emission line is expected to be $\gtrsim$10 times brighter than these other lines (e.g., Brauher et al. 2008), so we expect contamination to be modest given the shallow depth of the current ALMA data.

We investigate potential contamination using the multi-wavelength data available in the UDS field. The photometric properties of our emission line SMGs are given in Table 2. Most sources are very red or undetected in the optical/near-infrared, which is consistent with them being $z > 4$ dusty galaxies. In addition, only two have detections at 1.4 GHz, again consistent with the majority being at $z \gg 3$ (Chapman et al. 2005). A discussion of each of the individual line emitters is given in Appendix B.

Galaxies at $z \sim 4.5$ are not expected to be detected in the optical B-band due to the Lyman limit at 912 Å redshifting to $\gtrsim$5000 Å. In Figure 2 we show the high-resolution ALMA 870 μm continuum emission contoured over a B-band (or K-band) image of each galaxy. Half of the ALMA detections do not have a B-band counterpart and/or have photometric redshifts consistent with a $z > 4$ galaxy. The other five line emitters have B-band counterparts that are offset by $\lesssim$1 arcsec from the ALMA continuum emission. In these cases, we have flagged the photometry and note that this may indicate lensing of the submillimeter source by a foreground galaxy. These five sources are listed in italics in Table 2 and by circle symbols in all figures where the sources are individually plotted.

On the basis of their multi-wavelength properties, three of these five sources with nearby B-band counterparts appear to be potentially lensed high-redshift [C II] emitters, as the B-band emission is not spatially coincident with the submillimeter emission. We crudely estimate that the lensing of these sources may affect our measured fluxes by a factor of $\lesssim$1.5–2; however, with the current data we are unable to estimate more precise magnification factors.

We next estimate the line luminosities of the two sources where the submillimeter emission is spatially coincident (within 0.″5) with a B-band detection: AS2UDS.0243.0 and AS2UDS.0535.0, assuming these correspond to high-J ^{12}CO lines. We compare these luminosities to other studies of high-J ^{12}CO emission lines to see whether it is plausible that these lines are high-J ^{12}CO rather than [C II].

The photometric redshifts of AS2UDS.0243.0 and AS2UDS.0535.0 are reported in Table 2. At these redshifts the emission lines would correspond to CO(8–7) at $z = 1.63 \pm 0.01$ with $L_{\mathrm{CO(8-7)}} = 1.5 \times 10^8\ L_\odot$ for AS2UDS.0243.0 and CO(5–4) at $z = 0.70 \pm 0.01$ with $L_{\mathrm{CO(5-4)}} = 0.2 \times 10^8\ L_\odot$ for AS2UDS.0535.0. These luminosities are approximately an order of magnitude brighter than what is found in typical local ULIRGs (e.g., Arp 220; Rangwala et al. 2011) or AGN-dominated sources (e.g., Mrk 231; van der Werf et al. 2010). However, recent studies have found comparably luminous sources at higher redshifts ($z > 2$, e.g., Barro et al. 2017; Yang et al. 2017). It is therefore possible that these two sources lie at

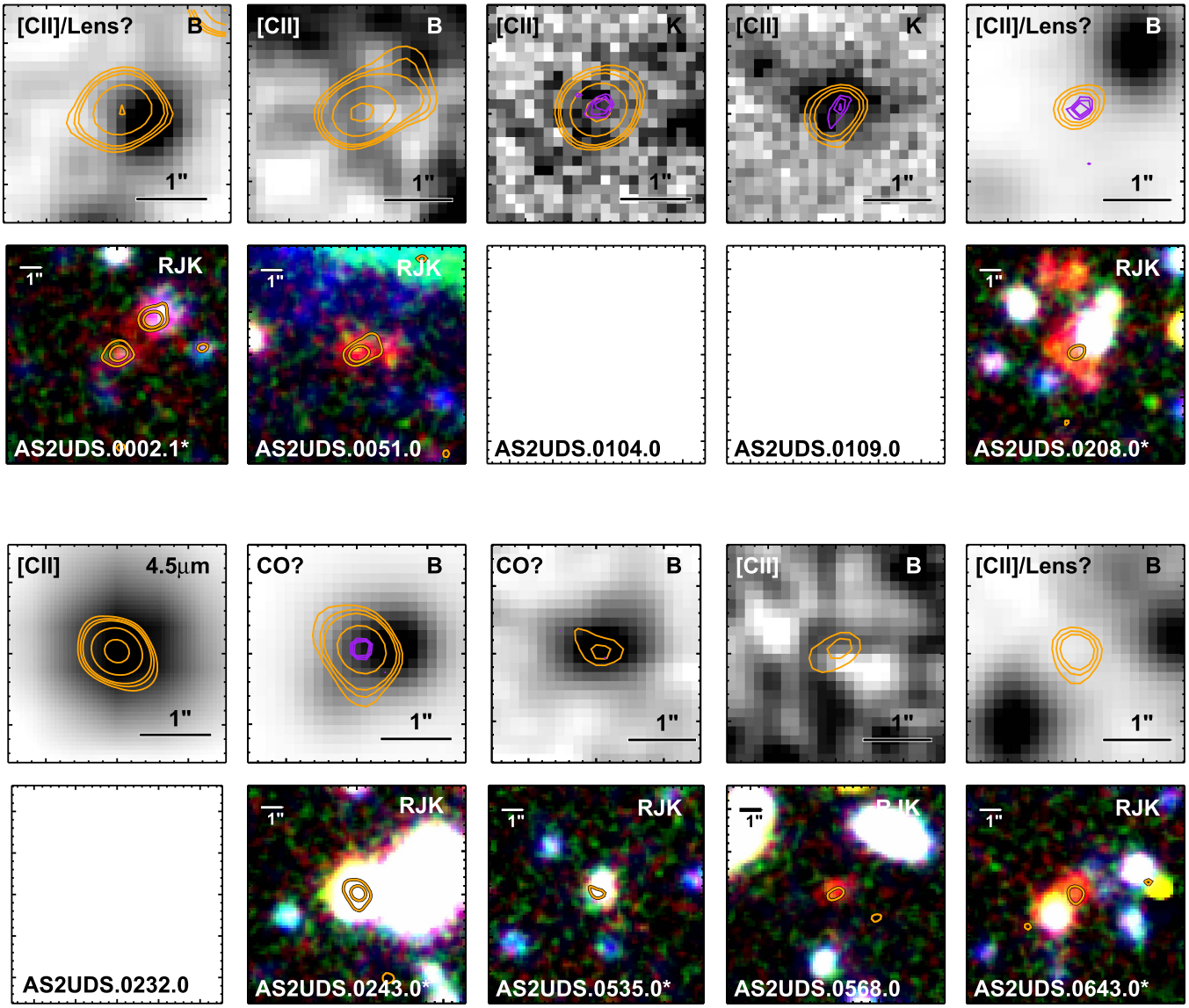

Figure 2. Thumbnails of the line emitters detected in our survey. Top row in each panel: $3'' \times 3''$ thumbnails with ALMA continuum contours overlaid at 3, 4, 5, 10, and 20σ on background images. These show the *B*-band unless the *B*-band is not available, in which case they show the *K* or IRAC 4.5 μm bands. Purple contours are high-resolution ALMA continuum maps ($\sim 0\farcs15$) where it is available, orange are at the tapered $0\farcs5$ resolution. Bottom row in each panel: $10'' \times 10''$ true color *R*, *J*, *K* thumbnails of the line emitters where available. All thumbnails are centered on the tapered ALMA continuum emission, shown by the orange contours at 3 and 10σ. We label each pair of panels with the source ID and our classification of the source (see Table 2); asterisks indicate that the photometry of the ALMA source may be contaminated by a foreground galaxy, lensed, or that the galaxy actually lies at $z < 4$ and the detected line is not [C II] (see discussion in Section 3.1).

$z < 4$, although they require further investigation to confirm the identity of the emission lines.

The majority ($\gtrsim$80%) of our detected emission lines appear to be [C II] at $z \sim 4.5$. Two have multi-wavelength properties that suggest they are lower-redshift CO emission. However, with no additional detected lines we cannot confirm the identity of the line emission in any of these sources. We therefore proceed with our analysis using all 10 line emitters. To guide the reader, in all plots we highlight SMGs that may lie at $z < 4$ or whose photometry could be affected by lensing. We also list these sources in italics in all tables. We have tested our conclusions by removing the two potential CO emitters and incorporate the removal of these sources into our error estimates. We find that the majority of our conclusions do not qualitatively change and our estimated quantities do not vary by more than the quoted errors. Any differences are noted in the relevant sections.

3.2. *[C II] Luminosities and Line Widths*

Figure 3 shows the FWHM and emission line luminosities of our 10 sources (with those that are potentially lower-redshift or lensed flagged) compared to other studies of high-redshift star-forming galaxies and AGNs. The FWHMs of the lines have a range of 200–800 km s^{-1}, with a median of 370 $\pm$ 50 km s^{-1}. This is similar to the values found in other high-redshift studies: Wang et al. (2013) estimate an average FWHM of $\sim$360 km s^{-1} in a sample of five $z > 6$ quasars and Gullberg et al. (2015) measure a range of 210–820 km s^{-1} in 20 strongly lensed star-forming galaxies at $2.1 < z < 5.7$. Three of our ten sources have a FWHM of $>$500 km s^{-1}, which is a similar fraction to that measured in Gullberg et al. (2015).

As discussed in Section 2.1, the false-positive rate for our sample is a function of velocity binning and line FWHM. In Figure 3 we therefore plot the 1σ limit for false-positive

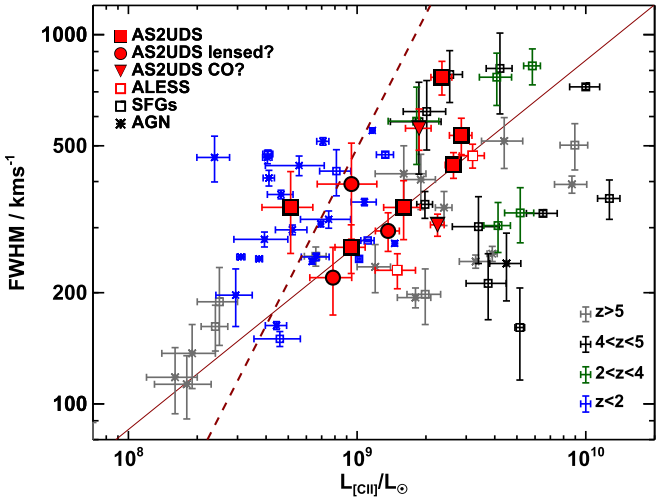

Figure 3. [C II] FWHM vs. line luminosity for the AS2UDS [C II] emitters. We compare our sample to star-forming galaxies and AGNs from the literature. The dashed line shows the 1σ limit for false positives in the AS2UDS sample (i.e., 84% of false positives lie to the left of this line). The solid line shows a FWHM $\propto L_{[\mathrm{C\,II}]}^{0.5}$ relation scaled to the median of the AS2UDS data points. This roughly reproduces the trend between the dynamics and luminosity seen in the data, which suggests the line luminosity reflects the mass of the system. Note that potentially lensed sources do not appear offset in luminosity at fixed FWHM, suggesting any lens amplification is modest. The literature values come from Iono et al. (2006), Venemans et al. (2012), Wang et al. (2013), Farrah et al. (2013), De Breuck et al. (2014), Gullberg et al. (2015), Willott et al. (2015), Miller et al. (2016), and Venemans et al. (2016).

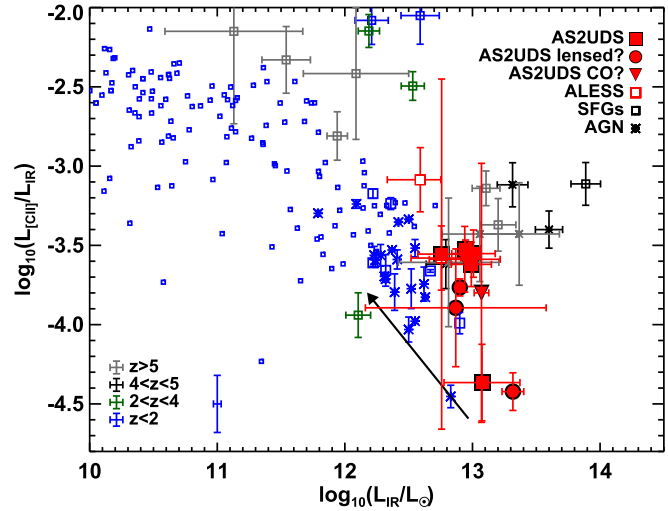

Figure 4. Ratio of [C II] luminosity to total IR luminosity assuming a fixed dust temperature of 50 K for the AS2UDS [C II] emitters compared to samples of AGNs and star-forming galaxies (SFGs) at $0 < z < 6.4$ from the literature. Also plotted are the ALESS sources from Swinbank et al. (2012; with updated luminosities from Swinbank et al. 2014). Our new $z \sim 4.5$ sample displays a continuation of the local trend of decreasing [C II] contribution to the total infrared luminosity toward higher luminosities, contrary to previous high-redshift studies. The arrow shows the effect of a change in dust temperature from 50 K, the median of the AS2UDS sample, to 35 K, commonly assumed in $z = 2$ SMG studies. The literature samples come from Farrah et al. (2013), Brisbin et al. (2015), Gullberg et al. (2015), and Capak et al. (2015). Low-redshift ($z < 2$) sources shown by small symbols are taken from Gullberg et al. (2015). A typical uncertainty for these low-redshift sources is shown in the lower left.

emission lines in our sample (shown by the dashed line). This is determined from the inverted spectra as described in Section 2.1; 84% of the false-positive emission lines lie to the left of this line.

The [C II] luminosity reflects a mixture of the mass of the gas reservoir and the star formation rate of the SMGs (though see Fahrion et al. 2017), whereas the FWHM is expected to trace their dynamical mass. The solid line in Figure 3 shows a model assuming the line-luminosity primarily traces dynamic mass: a FWHM $\propto L_{[\mathrm{C\,II}]}^{0.5}$ relation scaled to the median of the AS2UDS data points. This roughly reproduces the trends seen in the data, albeit with large scatter.

3.3. [C II] Deficit

Previous studies of local star-forming galaxies have found that the ratio of the [C II] to infrared luminosities declines toward higher infrared luminosities, resulting in a "[C II] deficit" in local ULIRGs (Figure 4; e.g., Stacey et al. 1991; Malhotra et al. 2001; Luhman et al. 2003). Several possible models have been proposed to explain this factor of $\sim$100 decline in [C II] line-luminosity fraction across three orders of magnitude in L_{IR}, including enhanced contributions from AGN to the total infrared luminosity in the most luminous galaxies, or high-ionization regions contributing more to continuum emission (e.g., Luhman et al. 2003; Sargsyan et al. 2012). At higher redshifts, however, ULIRGs and dusty star-forming galaxies appear to have $L_{[\mathrm{C\,II}]}/L_{\mathrm{IR}}$ ratios that are comparable to those of less-luminous $z \sim 0$ star-forming galaxies (e.g., Stacey et al. 2010; Cox et al. 2011; Swinbank et al. 2012; Walter et al. 2012). This poses the question of whether the processes responsible for [C II] emission at $z \gg 0$ differ from those occurring locally.

To investigate the "[C II] deficit" we must first estimate the infrared (rest-frame 8–1000 μm) luminosities of our line emitters. To do this we fit a modified blackbody to the far-infrared photometry of each source from *Herschel* PACS, SPIRE, and ALMA (e.g., as in Swinbank et al. 2014), adopting a spectral index[20] of $\beta = 1.8$ (e.g., Béthermin et al. 2015).

Using this modified blackbody SED we estimate infrared luminosities ranging between $L_{\mathrm{IR}} = (7\text{–}34) \times 10^{12}\,L_\odot$ for the AS2UDS emission line sources. The derived characteristic dust temperatures are 39–77 K. Table 3 lists their infrared luminosities, dust temperatures, [C II] equivalent widths (EWs), and luminosities. The EWs are derived using continuum values from the median of the fit to the full spectrum (derived in Section 2.1).

As expected, few of the candidate line emitters are individually detected in the *Herschel* bands (Table 2) due to their relative faintness and potentially high redshifts, so while we can fit the PACS/SPIRE/ALMA fluxes for each individual source with a modified blackbody, these are very uncertain. We therefore also construct an average SED for the whole sample by stacking the individual, un-deblended *Herschel* images at the positions of the ALMA line emitters and extracting bootstrap mean fluxes.[21] In Figure 5 we show the stacked sample in the *Herschel* PACS 100, 160 μm and SPIRE 250, 350, and 500 μm bands. Fitting a modified blackbody SED to the stack gives a median infrared luminosity $L_{\mathrm{IR}} = (1.0 \pm 0.4) \times 10^{13}\,L_\odot$, assuming the sources lie at $z = 4.45$ (the median redshift of our sample), and a median dust temperature of $T_{\mathrm{d}} = 51 \pm 4$ K, where the uncertainty is

[20] Varying the spectral index over $1.5 < \beta < 2.3$ changes the luminosities by $\leqslant$0.06 dex and temperatures by 12 K (decreasing with larger β).

[21] Using bootstrap median fluxes does not change our derived quantities outwith the quoted errors. The infrared luminosities decrease by 0.03 dex.

Table 3
[C II] Emitter Derived Properties

Source ID	L_{IR} (10^{12} $L_\odot$)	$L_{IR,freeTd}$ (10^{12} $L_\odot$)	T_d (K)	$L_{[C\,II]}$ (10^8 $L_\odot$)	$EW_{[C\,II]}$[a] (km s^{-1})
AS2UDS.0002.1[b]	21 ± 4	24 ± 4	53 ± 3	8 ± 2	200 ± 50
AS2UDS.0051.0	10 ± 3	7 ± 3	40 ± 6	24 ± 3	580 ± 70
AS2UDS.0104.0	10 ± 3	7 ± 3	41 ± 6	29 ± 3	1050 ± 140
AS2UDS.0109.0	9 ± 1	8 ± 1	44 ± 7	26 ± 2	1100 ± 310
AS2UDS.0208.0[b]	8.0 ± 0.2	7.7 ± 0.2	48 ± 9	14 ± 2	650 ± 240
AS2UDS.0232.0	12 ± 6	18 ± 6	57 ± 3	5 ± 1	210 ± 60
AS2UDS.0243.0[b,c]	<22	34 ± 22	72 ± 11	19 ± 2	850 ± 160
AS2UDS.0535.0[b,c]	9 ± 4	13 ± 4	62 ± 8	23 ± 2	2200 ± 800
AS2UDS.0568.0	<6	20 ± 15	77 ± 10	16 ± 3	2300 ± 1300
AS2UDS.0643.0[b]	7 ± 6	13 ± 6	64 ± 7	9 ± 3	700 ± 260
Median values[d]	9.3 ± 0.4	13.1 ± 0.9	55 ± 4	17.3 ± 0.8	770 ± 70
Supplementary catalog					
AS2UDS.0109.1	<7.0	<8.0	<55	7.6 ± 1.2	900 ± 500

Notes. Two values of L_{IR} are listed: the value obtained from fitting the far-infrared SED with a modified blackbody with a fixed dust temperature of 50 K, and, in brackets, the value obtained if dust temperature is left as a free parameter.
[a] Equivalent widths are given in the rest-frame.
[b] Italics indicates that the source has a nearby companion that may contaminate the photometry.
[c] AS2UDS.0243.0 and AS2UDS.0535.0 have photometric properties that indicate the line we detect may instead be CO(8–7) or CO(5–4) respectively, corresponding to $z_{CO} < 2$. Further observations are needed to confirm the nature of these emission lines.
[d] Uncertainties on median values are the standard error.

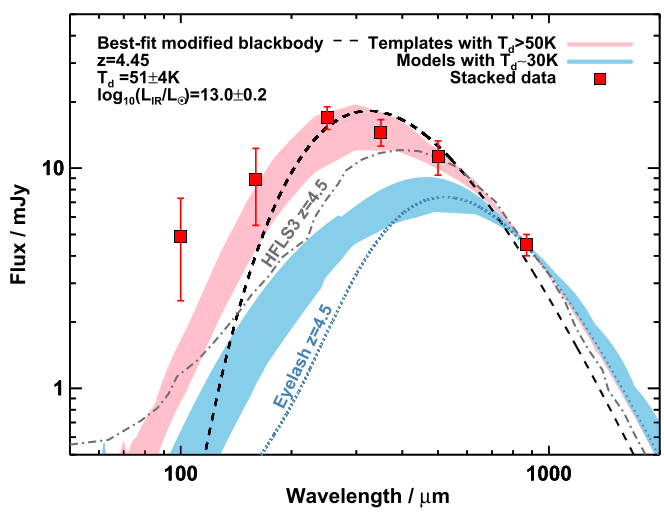

Figure 5. Composite infrared SED from *Herschel* PACS/SPIRE and ALMA for our 10 line emitters with uncertainties determined from a bootstrap analysis. The dashed black line shows the best modified blackbody fit to this photometry with $\beta = 1.8$. The best-fit parameters are shown in the top left. Overlaid are shaded regions showing the region occupied by template SEDs with temperatures $T_d > 50$ K and 28 K $< T_d <$ 35 K. The SED of our AS2UDS SMGs at $z \simeq 4.5$ suggests warm dust temperatures for these high-redshift galaxies. Also plotted are the SEDs of two well-studied SMGs, SMMJ2135−0102 (the Eyelash; Swinbank et al. 2010b), and HFLS3 (Riechers et al. 2013; Cooray et al. 2014), redshifted to $z = 4.5$ and normalized to the average flux density of our sample at 870 μm.

taken from a bootstrap analysis that excludes those sources that may be foreground CO emitters.

Figure 4 shows the $L_{[C\,II]}/L_{IR}$ ratio versus L_{IR} for the AS2UDS line emitters, compared to local and other high-redshift samples. We note that although our measured [C II] fluxes (and hence luminosities) have been corrected for the ALMA primary beam, the spectra are measured from the brightest pixel in the tapered map, whereas the infrared luminosities are derived from (aperture-corrected) continuum 1 arcsec aperture fluxes (S. M. Stach et al. 2018, in preparation). As all fluxes are measured from 0.5 arcsec tapered images/cubes, the effect of the different methods on our measured line fluxes is likely to be modest. We tested this by extracting spectra from a similar aperture and find that, although there is significant scatter between different galaxies, this effect may cause our [C II] luminosities (and therefore $L_{[C\,II]}/L_{IR}$ ratios) to be low by 0.2–0.3 dex.

We compare our sample with local galaxies from Graciá-Carpio et al. (2011) and Herrera-Camus et al. (2018). These sources include LIRGs and ULIRGs from the Great Observatories All-sky LIRG Survey (Díaz-Santos et al. 2013) and normal and Seyfert galaxies from Brauher et al. (2008). The median $L_{[C\,II]}/L_{IR}$ ratio for our $z \sim 4.5$ [C II] emitters ∼0.02%, similar to those of local ULIRGs, although the AS2UDS sources have higher infrared luminosities. Our measured ratios are in agreement with those of Swinbank et al. (2014) for their two [C II] emitters at $z = 4.4$, however, we measure lower ratios than have been suggested in previous high-redshift studies by Gullberg et al. (2015), Capak et al. (2015), or Brisbin et al. (2015). This is a consequence of the relatively warm dust temperatures we estimate for our $z \sim 4.5$ SMGs. If we fix the dust temperature for our [C II] emitters to ∼35 K (as is typically found in $z \sim 2$ SMGs) their estimated infrared luminosities decrease by approximately 0.6 dex, which is shown by the arrow in Figure 4. However, this cooler SED does not match well to the measured photometry (for example, at 350 μm the required flux density is a factor of two lower than we measure; Figure 5, Section 3.5).

The [C II] deficit is known to be strongly correlated with infrared surface brightness, or equivalently star formation surface density (Díaz-Santos et al. 2014; Lutz et al. 2016; Smith et al. 2017). Thus, our measured high dust temperatures and large [C II] deficit may both be explained if our $z \sim 4.5$ SMGs have high star formation rate surface densities, compared to previously studied sources.

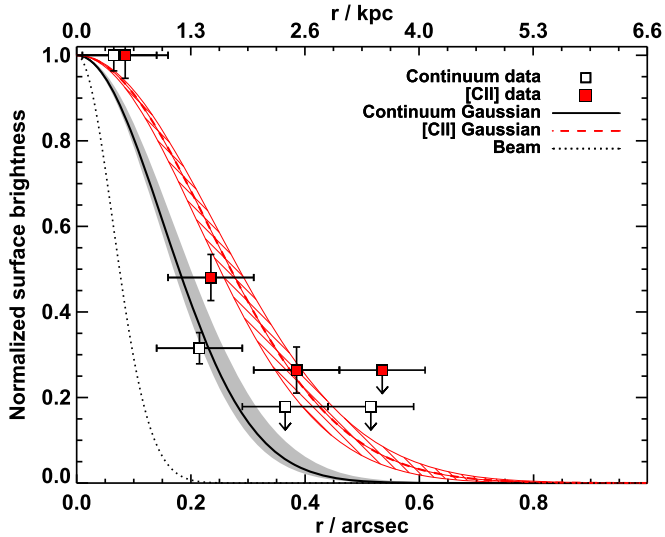

Figure 6. Average radial profiles of the dust continuum and [C II] emission in our SMGs from the stacked images. The solid black and dashed red lines show the profile derived using a 2D Gaussian fit to the stacked data for continuum and [C II] emission, respectively. The profiles have been normalized to compare them: the [C II] emission is more extended than the continuum emission. Uncertainties on the Gaussian profiles were determined using a bootstrap analysis. Error bars on the abscissae show the size of the radial bins. The points have been offset by $\pm 0\farcs01$ for clarity. 2σ limits are shown for non-detections. The dotted line shows the ALMA beam profile for reference.

3.4. Sizes of [C II] Emitters

Previous studies of [C II] emission line sources have suggested that the [C II] emission is more extended than the dust continuum emission in high-redshift SMGs (e.g., Gullberg et al. 2018, with a sample of four $L_{\rm IR} \sim 3 \times 10^{12}\,L_\odot$ SMGs at $z \sim 4.5$).

Six out of our ten line emitters were observed with ALMA in an extended configuration, resulting in maps with synthesized beam FWHM of $\sim 0\farcs15$, or 1 kpc at $z = 4.5$. We use these data to investigate the sizes of our [C II] emitters. To measure an average size for their dust continuum and [C II] emission, we stacked the continuum and [C II] emission of the six [C II] emitters with high-resolution data.[22] For the continuum stack, each individual map was normalized to a peak flux of unity to avoid brighter sources dominating the size measurements. [C II] images were constructed from the emission within ± 1 FWHM in frequency of the emission line peak, continuum-subtracted, and then similarly normalized. We find no spatial offset between the peaks of the two stacks (Δdust–[C II] $<$ 0.06 arcsec) and no asymmetry in either stack. Using a two-dimensional Gaussian profile fit we measure circularized effective radii (deconvolved with the beam) of $0.15^{+0.02}_{-0.01}$ arcsec and $0.25^{+0.01}_{-0.04}$ arcsec (corresponding to 1.0 ± 0.1 kpc and $1.7^{+0.1}_{-0.2}$ kpc at $z \sim 4.5$) for the continuum and [C II] stacks, respectively (Figure 6, where the errors come from bootstrapping). This demonstrates that the [C II] emission is significantly more extended than the continuum emission in these $z = 4.5$ galaxies; we find [C II] sizes similar in extent to the continuum in just $\sim$5% of the bootstrap simulations. Our measured sizes are in agreement with those from previous studies at this redshift of SMGs (e.g., Gullberg et al. 2018), as well as quasars (e.g., Kimball et al. 2015; Díaz-Santos et al. 2016), although smaller by a factor of $\sim$2 compared to higher-redshift Lyman break galaxies (Capak et al. 2015). This may indicate that our $z \sim 4.5$ SMGs are more compact starbursts than $z > 5$ Lyman break galaxies.

Our sample of 10 SMGs has a median infrared luminosity of $(9.3 \pm 0.4) \times 10^{12}\,L_\odot$. This corresponds to a median SFR $= 1600 \pm 200\,M_\odot\,{\rm yr}^{-1}$, (using a Salpeter (1955) initial mass function; Kennicutt 1998). With our continuum sizes measured above, this gives a star formation rate surface density of $130 \pm 20\,M_\odot\,{\rm yr}^{-1}\,{\rm kpc}^{-2}$. This value is slightly higher than that measured in $z \sim 2.5$ SMGs ($90 \pm 30\,M_\odot\,{\rm yr}^{-1}\,{\rm kpc}^{-2}$; Simpson et al. 2015) and may indicate that our SMGs follow the trend found in Smith et al. (2017) of an increasing [C II] deficit with increasing star formation rate surface density. For a review of possible physical explanations we refer the reader to Smith et al. (2017), who found that this is likely caused by local physical processes of interstellar gas rather than global galaxy properties such as total luminosity.

We also fit the sizes of the galaxies in the near-infrared UKIDSS/UDS DR11 K-band image, to trace the stellar emission, using GALFIT/GALAPAGOS (Peng et al. 2002; Barden et al. 2012). Further details of the UDS K-band Sérsic fitting can be found in Almaini et al. (2017; see also Lani et al. 2013). We were able to obtain fits for four of our ten[23] emitters. The remaining SMGs were either too faint in the K-band or were blended with other nearby sources. These four galaxies give a median (deconvolved) size that is considerably more extended than both the dust and [C II] emission: 0.7 ± 0.1 arcsec radius (4.7 ± 0.7 kpc). This is slightly larger than the values found in studies of *Hubble Space Telescope* H_{160} sizes of SMGs at $1 < z < 3.5$, which measure half-light radii of $\sim 2.7 \pm 0.4$ kpc (Swinbank et al. 2010a; Chen et al. 2015). The K-band fits also output a median Sérsic index $n = 0.80 \pm 0.06$, consistent with a disk profile. This suggests that the stars visible in the rest-frame UV are more extended than the dust-obscured starburst region in these systems. This may suggest that we are seeing highly dissipative starbursts occurring within pre-existing stellar systems.

3.5. $z \sim 4.5$ SMGs are Warm

Comparing their inferred dust temperatures and far-infrared luminosities in Figure 7, our sample of $z \sim 4.5$ SMGs appears to have warmer characteristic dust temperatures at fixed luminosity than inferred for $z \simeq 2$ SMGs and star-forming galaxies (e.g., Magnelli et al. 2012a; Symeonidis et al. 2013; Swinbank et al. 2014; da Cunha et al. 2015, but see also Casey et al. 2012). In this section we first test the reliability of our measured dust temperatures and then discuss the implications of warm dust temperatures on the selection of high-redshift SMGs.

We first note that at $z \sim 4.5$ the temperature of the cosmic microwave background (CMB) is $\sim$15 K and this can bias temperature measurements of high-redshift galaxies (da Cunha et al. 2013). However, the temperatures we measure for our [C II] emitters, $T_{\rm d} = 39$–77 K, are 2.5–5$\times$ warmer than the CMB, so this is unlikely to significantly affect our measurements.

Warmer characteristic dust temperatures correspond to the far-infrared SED peaking at shorter wavelengths. For a $z = 4.5$

[22] AS2UDS.0104.0, AS2UDS.0109.0, AS2UDS.0208.0, AS2UDS.0232.0, AS2UDS.0243.0, and AS2UDS.0535.0: the measured profiles do not change if we remove the two potential low-redshift emitters.

[23] AS2UDS.0051.0, AS2UDS.0109.0, AS2UDS.0535.0, AS2UDS.0568.0: the median size does not change if we remove AS2UDS.0535.0.

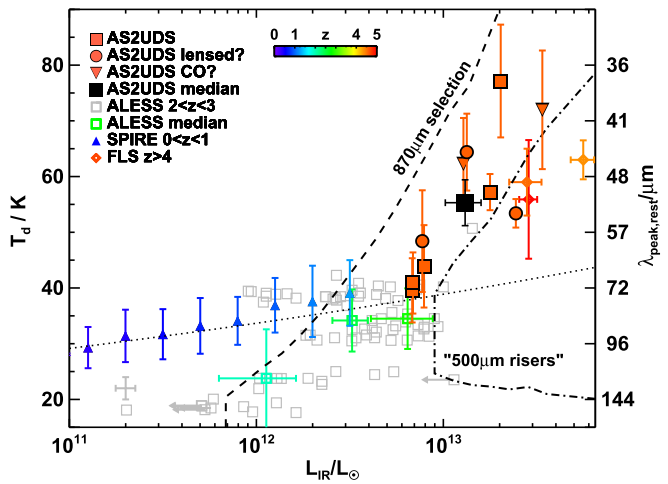

Figure 7. Dust temperature ($T_{\rm d}$) as a function of total infrared luminosity ($L_{\rm IR}$) for the line emitters in our survey, color-coded by redshift. At a given redshift, the characteristic dust temperature roughly corresponds to the wavelength at which a galaxy's SED peaks. Individual line emitters are shown, as well as the median of the sample. The $z \simeq 4.5$ AS2UDS candidate [C II] emitters have warmer dust temperatures, or equivalently their dust SEDs peak at shorter wavelengths, at fixed luminosity compared to $z \simeq 0$ galaxies. For comparison we also show ALESS SMGs from Swinbank et al. (2014) (a typical error bar is shown in the lower left), with median values overplotted and color-coded by redshift. Binned low-redshift SPIRE-selected (U)LIRGs from Symeonidis et al. (2013) are shown by the solid triangles. We indicate the low-redshift correlation by the dotted line. The dashed line shows the approximate selection limit for an 870 μm selected sample with $S_{870} > 3.6$ mJy: sources to the right of this line would be detected. The dotted–dashed line shows the approximate selection limit for $4 < z < 6.5$ sources whose SED peaks at $\lambda \geqslant 500$ μm, so-called "500 μm risers" (Dowell et al. 2014): sources to the right of this line would be selected. Plotted for comparison are three such sources, with spectroscopic redshifts $z > 4$, from the First Look Summary (FLS) of the *Herschel* Multi-tiered Extragalactic Survey (HerMES; Oliver et al. 2012).

SMG, the *Herschel* PACS/SPIRE wavebands correspond to $\lesssim$90 μm rest-frame. This means that our measurement of cold dust in these SMGs is dominated by the 870 μm flux measurement (rest-frame 160 μm). To test whether having only one data point at longer wavelengths may bias our measurements toward warmer measured dust temperatures, we use simulated SEDs for galaxies with a range of known dust temperatures and infrared luminosities, redshifted to $z = 4.5$. Convolving these simulated SEDs with the *Herschel*/ALMA observational wavebands and applying the flux limits appropriate for our observations, we then measure "observed" dust temperatures. We find the measured dust temperatures agree with the input temperatures, with $|T_{\rm d,in} - T_{\rm d,out}|/T_{\rm d,in} = 0.07$ on average. Our measured temperatures are therefore not a consequence of the coverage of our observations.

From Figure 5 we see that, as with the individual sources, the measured average dust temperature for the composite SED is warm compared to typical temperatures of $\sim$32 $\pm$ 1 K estimated for SMGs at lower redshifts (Swinbank et al. 2014). This is due to the higher average infrared luminosity in the $z \sim 4.5$ sample; Swinbank et al. (2014) measured $L_{\rm IR} = (3.0 \pm 0.3) \times 10^{12}\,L_\odot$ at $z \sim 2.5$, compared to our value of $L_{\rm IR} = (1.0 \pm 0.4) \times 10^{13}\,L_\odot$. As the far-infrared SED of distant galaxies can be reasonably approximated by modified blackbody emission, the infrared luminosity is proportional to dust mass and temperature as $L_{\rm IR} \propto M_{\rm d} T_{\rm d}^{4+\beta}$. We measure similar sizes for the continuum emission in our $z \sim 4.5$ SMGs as at $z \sim 2.5$: 2.4 $\pm$ 0.2 kpc (Simpson et al. 2015). As infrared luminosity traces star formation rate, and dust mass is correlated with the radius of the dust-emitting region, the higher average luminosity and similar average radius correspond to a higher star formation rate surface density, which explains the high temperatures observed in our sample.

Significant effort has been invested into identifying dusty star-forming galaxies at $z \gtrsim 4$ using *Herschel*/SPIRE (e.g., Roseboom et al. 2012; Dowell et al. 2014; Yuan et al. 2015; Asboth et al. 2016). We investigate whether our blind [C II] detections in a 870 μm survey would be identified by these other selections. Figure 7 shows two selection limits: first, SMGs that are brighter than $S_{870} \simeq 3.6$ mJy ("870 μm selection"). Second, we show the selection of sources with $S_{500} > 30$ mJy and $S_{500} > S_{350} > S_{250}$, i.e., a red "500 μm riser" (e.g., Dowell et al. 2014). The latter would select one of our [C II] emitters (AS2UDS.0002.1, which may be lensed), but would miss most of our sample as they are too faint at 500 μm. If it was possible to go $\sim$2–3 times deeper at 500 μm, then the "500 μm riser" selection would have identified all our candidate [C II] emitters.

3.6. Molecular and Dynamical Masses of $z \gtrsim 4$ [C II] Emitters

SMGs have high star formation rates and are believed to have large cold gas reservoirs (Bothwell et al. 2013). The mass of cold gas available places constraints on the duration of the starburst, which has implications for the predicted number densities of SMGs.

The cold gas mass can be estimated from the dust mass of a galaxy by adopting a suitable gas-to-dust ratio. Previous studies of the gas-to-dust ratio in star-forming galaxies and SMGs have found a range of values: for example, in local star-forming galaxies the gas-to-dust ratio is higher (GDR = 130 $\pm$ 20; Draine et al. 2007), whereas in the ALESS sample Swinbank et al. (2014) estimate a gas-to-dust ratio of GDR = 75 $\pm$ 10 using the correlation between stellar mass, metallicity, and star formation rate from Maiolino et al. (2008; see also Magnelli et al. 2012b). From fitting the far-infrared SEDs of the ALESS sample, Magnelli et al. (2012a) suggested a slightly higher average gas-to-dust ratio of GDR = 90 $\pm$ 25. The gas-to-dust ratio is also a function of metallicity and has been suggested, from studies of a small number of SMGs, to decrease toward higher redshifts (e.g., Ivison et al. 2010; Santini et al. 2010).

We estimate the dust masses for our SMGs using

$$M_{\rm d} = \frac{S_{870} D_{\rm L}^2}{\kappa B_\nu (1+z)}, \qquad (1)$$

where B_ν is the Planck function, $D_{\rm L}$ is the luminosity distance, S_{870} is the flux density at rest-frame 870 μm, extrapolated assuming $\beta = 1.8$, $\kappa = 0.077\ {\rm m^2\,kg^{-1}}$ (Dunne et al. 2000) and the values of $T_{\rm d}$ and $z_{\rm [C\,II]}$ derived in Section 3.3. We obtain an average dust mass $M_{\rm d} = (1.6 \pm 0.3) \times 10^8\,M_\odot$, although we note that the measured dust mass is a strong[24] function of β and $T_{\rm d}$. This dust mass is similar to those found in previous surveys at $z \leqslant 4$ (e.g., Swinbank et al. 2014; da Cunha et al. 2015). Adopting the value of GDR = 90 $\pm$ 25 from Magnelli et al. (2012a) then predicts gas masses of $M_{\rm gas} = (1.5 \pm 0.5) \times 10^{10}\,M_\odot$.

To obtain a gas fraction for our sample, we estimate total masses from dynamical measurements of the [C II] line. From

[24] The dust mass varies from (0.5–2.7) $\times 10^8\,M_\odot$ for $\beta = 2.4$–1.5.

the median size of the [C II] emission region in our sample ($r_e = 1.7 \pm 0.2$ kpc), and the median line width of FWHM $= 370 \pm 50$ km s^{-1} (Table 1), we can estimate a dynamical mass using a disk model for the [C II] line dynamics:

$$M_{\rm dyn} = \frac{1}{\sin^2(i)}\frac{v^2 r_e}{G}, \quad (2)$$

where v is the line width, r_e is the effective radius, and G is the gravitational constant. Assuming the average value for randomly inclined galaxy disks $\langle \sin i \rangle = 0.79$ (Law et al. 2009) gives $M_{\rm dyn} = (2.1 \pm 0.6) \times 10^{10}\, M_\odot$.

To scale our measured total gas masses to the gas enclosed within $r_e = 1.7$ kpc, and thus directly compare them to the calculated dynamical mass, we assume the cold gas reservoir is similar in scale to the [C II] emission and scale the gas mass by the fraction of [C II] emission within the effective radius: 50%. With this we estimate a typical gas fraction of $f_{\rm gas} = 0.5 \times M_{\rm gas}/M_{\rm dyn} = 0.4 \pm 0.2$. This is consistent with the value predicted for $z = 4.5$ galaxies by Tacconi et al. (2018) of $f_{\rm gas} \sim 0.4$ and the $z \sim 4$ value estimated in Béthermin et al. (2015) of $f_{\rm gas} = 0.65^{+0.16}_{-0.29}$. We caution that this value is highly dependent upon the adopted gas-to-dust ratio and measured dust and dynamical masses, each of which have large uncertainties and require further detailed observations to confirm.

3.7. [C II] Luminosity Function

The evolution of the number density and luminosity of [C II] emitters as a function of redshift provides information on the evolution of the star formation rate density. This is particularly useful at $z > 4$, where the contribution of dust-obscured galaxies to the cosmic star formation rate density is still relatively unconstrained (e.g., Madau & Dickinson 2014).

With our sample of SMGs we can calculate a [C II] luminosity function at $z \simeq 4.5$. Here, we only use those with continuum flux densities of $S_{870} \geqslant 3.6$ mJy, as our continuum survey is complete to this level. We therefore use seven of our SMGs (Table 1). We first correct for incompleteness in our sample: from inserting 10^4 false emission lines into spectra where no lines were originally detected and re-running our emission line detection we determine the recovery rate of emission lines as a function of line luminosity. From this analysis we find completeness rates of 90% at $L_{\rm [C\,II]} > 2.3 \times 10^9\, L_\odot$, 80% at $L_{\rm [C\,II]} > 1.5 \times 10^9\, L_\odot$, 70% at $L_{\rm [C\,II]} > 8 \times 10^8\, L_\odot$, and 50% at $L_{\rm [C\,II]} > 3 \times 10^8\, L_\odot$. Our luminosity function has been corrected for these completeness rates. The lower luminosity bin has a completeness of $\lesssim$70%. We therefore plot a lower limit, as our correction is unlikely to account for the full incompleteness.

We note that our line emitters are not a simple [C II]-selected sample, as they were all selected to have a dust continuum detection. With the current samples of high-redshift SMGs available it is not currently possible to estimate how many [C II] emitters may be missed due to this selection. Our measured values are therefore likely to be a lower limit on the [C II] luminosity function. Removing the SMGs in our sample that are potential lenses or lower-redshift sources lowers our estimate at the bright end of the luminosity function by $<2\sigma$, so the following analysis remains qualitatively similar.

Since our ALMA survey observed all the $S_{850} \geqslant 4$ mJy SCUBA-2 Cosmology Legacy Survey submillimeter detections in the UDS, we use the full area of the field and the number of [C II] emitters to estimate the bright end of the [C II] luminosity function at $z \sim 4.5$. The UDS is a ~0.96 sq. degree field and our ALMA observations cover a redshift range $\Delta z = 0.12$, giving a comoving volume of 1.2×10^6 Mpc^3. Figure 8 shows the [C II] luminosity function at $z \sim 4.5$ as derived from our sample of seven $S_{870} > 4$ mJy continuum-selected [C II] emitters.

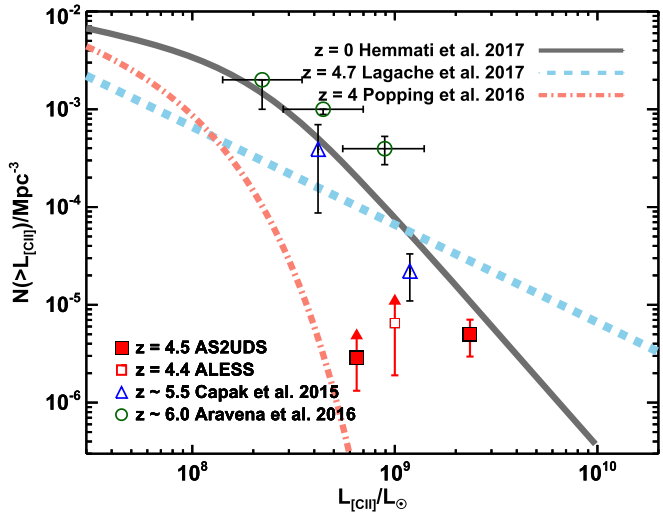

Figure 8. $z \sim 4.5$ [C II] luminosity function for the AS2UDS continuum-selected [C II] emitters compared to the ALESS sample from Swinbank et al. (2012) and higher-redshift studies from Capak et al. (2015) and Aravena et al. (2016). Overlaid are the $z = 0$ [C II] luminosity function measured in Hemmati et al. (2017), the $z = 4$ model from Popping et al. (2016), and the $z \sim 4.7$ model from Lagache et al. (2018). We note that our data points are a lower limit on the [C II] luminosity function as our sample are detected in both [C II] and the dust continuum. Our data are consistent with the measured limit from Swinbank et al. (2012) and with little-to-no evolution in the [C II] luminosity function since $z = 0$. The Popping et al. (2016) model underpredicts our observations, while the Lagache et al. (2018) model and Hemmati et al. (2017) $z = 0$ observations are consistent with our lower limit on the bright end of the [C II] luminosity function at this redshift.

Our measured [C II] luminosity function agrees well with the lower limit derived by Swinbank et al. (2012) and the estimated density of UV-selected $z \sim 5.5$ [C II] emitters from Capak et al. (2015). We find a lower number density than that measured in Aravena et al. (2016), whose values at $z \sim 6$ are upper limits, as the emission line sources in their sample are unconfirmed candidate [C II] emitters.

In Figure 8 we compare to the $z = 0$ [C II] luminosity function from Hemmati et al. (2017), the predicted $z = 4$ luminosity function from Popping et al. (2016), and the predicted form at $z = 4.7$ from Lagache et al. (2018). We find no evidence for any strong evolution of the [C II] luminosity function between $z = 0$ and $z \sim 4.5$, consistent with the prediction from Hemmati et al. (2017) that the [C II] luminosity function increases from $z = 0$ to $z = 2$ and decreases again thereafter.

Our observations at the bright end of the luminosity function suggest that the model of Lagache et al. (2018) overpredicts the [C II] luminosity function at this redshift unless our sample selection is incomplete, which is possible. By contrast, the Popping et al. (2016) model, as noted in that study, vastly underpredicts the observed number density of [C II] emitters at all luminosities. This is also true for their models at $z = 0$ and $z = 6$. The underprediction of the [C II] luminosity function may be due to the semi-analytic models producing gas

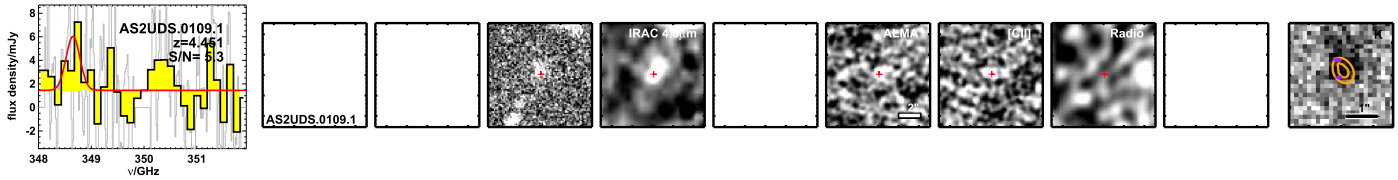

Figure 9. Spectrum and thumbnails for the supplementary [C II] emitter AS2UDS.0109.1. This is a continuum source in the same ALMA map as AS2UDS.0109.0, an 11σ line emitter at $z = 4.450$. Examining the same region of the spectrum in AS2UDS.0109.1 we find a tentative 5.3σ detection of an emission line, which would correspond to [C II] at $z = 4.451$. The photometric thumbnails where available are also shown. Without optical coverage it is difficult to determine, but the K and IRAC photometry is consistent with a $z > 4$ source. Further observations are required to confirm this companion source.

reservoirs in galaxies that are much less massive than expected (e.g., Popping et al. 2015), thus having star formation rates that are low and therefore lower [C II] luminosities.

We can also use our results to place limits on the redshift distribution of SMGs. We can use our sample to estimate the number density of $S_{870} \geqslant 3.6$ mJy sources at $z \simeq 4.5$ as 6–7 in 1.2×10^6 Mpc^3 (where the range indicates removing/retaining AS2UDS.0243.0 in the sample), yielding a space density of $\gtrsim$(5–6 $\pm$ 1) $\times 10^{-6}$ Mpc^{-3}. This indicates that $\sim$50–60/695 (7–8 $\pm$ 4%) of the SMGs in AS2UDS are expected to be at $z = 4$–5. This is consistent with Simpson et al. (2014), who found 35 $\pm$ 5% of SMGs in the ALESS survey lie at $z > 3$ (see also Danielson et al. 2017, who estimated that $\sim$23% of their spectroscopic SMG sample are at $z > 3$ and Michałowski et al. (2017) ,who estimated that 23% of SCUBA-2 submillimeter sources in the UDS are at $z \geqslant 4$).

4. Conclusions

We have used ALMA at 870 μm to observe a sample of 716 SCUBA-2-selected sources brighter than $S_{850} \geqslant 3.6$ mJy (4σ) in the UKIDSS UDS field. With high-resolution (0.″15–0.″30) ALMA observations we detect the SMG counterparts to the single-dish submillimeter sources. We use these data to identify bright line emitters that fall in the 7.5 GHz bandwidth of our ALMA observations. We detect 10 line emitters above an S/N of 7, corresponding to a false detection rate of 10% (as derived from inverting the datacubes). All of these line emitters are 870 μm continuum-detected sources in our parent survey with $S_{870} \gtrsim 1$ mJy. The majority of these line emitters have multi-wavelength properties consistent with [C II]λ 157.8 μm emitters at $z = 4.4$–4.6. Our main results are summarized below.

1. We detect 10 candidate line emitters, at least 8 of which are likely to be [C II] emitters at $z = 4.4$–4.6, placing a lower limit of $>5 \times 10^{-6}$ Mpc^{-3} on the space density of SMGs at $z = 4.5$, and suggesting $\geqslant$7% of $S_{870} \gtrsim 1$ mJy SMGs lie at $z > 4$.
2. The ratio of $L_{[\mathrm{C\,II}]}/L_{\mathrm{IR}}$ for our galaxies is similar to that seen in ULIRGs at $z \simeq 0$, even though the SMGs have infrared luminosities an order of magnitude higher.
3. Through stacking we find that the [C II] emission is 1.5$\times$ more extended than the continuum dust emission in $z \sim 4.5$ SMGs (1.7 kpc versus 1.0 kpc). The extended [C II] emission compared to the dust continuum together with the measured infrared luminosities in these SMGs combines to give a star formation rate surface density measurement of $130 \pm 20\, M_\odot\, \mathrm{yr}^{-1}\, \mathrm{kpc}^{-2}$. This high surface density of star formation may explain the large [C II] deficit, as shown in Smith et al. (2017); however, the origin of the [C II] deficit is complex and unlikely to be simply caused by one factor.
4. We find that the [C II] luminosity function at $z = 4.5$ is very similar to that at $z = 0$. The similar luminosity functions at $z = 4.5$ and $z = 0$ are consistent with the prediction from Hemmati et al. (2017) that the [C II] luminosity function increases up to $z \simeq 2$ and decreases again thereafter.

The authors thank the anonymous referee for their comments, which improved the flow and content of this paper. E.A.C., B.G., and I.R.S. acknowledge support from the ERC Advanced Investigator Grant DUSTYGAL (321334) and STFC (ST/P000541/1). I.R.S. also acknowledges support from a Royal Society/Wolfson Merit Award. J.L.W. acknowledges an STFC Ernest Rutherford Fellowship. M.J.M. acknowledges the support of the National Science Centre, Poland through the POLONEZ grant 2015/19/P/ST9/04010; this project has received funding from the European Union's Horizon 2020 research and innovation program under the Marie Skłodowska-Curie grant agreement No. 665778. This paper makes use of the following ALMA data: ADS/JAO. ALMA#2015.1.01528.S, ADS/JAO.ALMA#2016.1.00434. S. ALMA is a partnership of ESO (representing its member states), NSF (USA) and NINS (Japan), together with NRC (Canada), MOST and ASIAA (Taiwan), and KASI (Republic of Korea), in cooperation with the Republic of Chile. The Joint ALMA Observatory is operated by ESO, AUI/NRAO, and NAOJ.

Appendix A
Supplementary Source AS2UDS.0109.1

Some of our detected line emitters have continuum-detected companions within the ALMA primary beam. We searched the spectra of any companions for emission lines at the same frequency as our detected line. AS2UDS.0109.1 has a tentative 5.3σ detection of an emission line which would correspond to [C II] at $z = 4.451$. This would place it at the same redshift at AS2UDS.0109.0; however, the line is very weak and the false-positive rate at this significance and line width is $\sim$50%. Further observations are therefore required to confirm the line. The spectrum and photometric thumbnails for AS2UDS.0109.1 are shown in Figure 9.

Appendix B
Additional Data and Discussion of Candidate [C II] Emitters

Figure 10 shows 10″ $\times$ 10″ multi-wavelength thumbnails, plus an enlarged view of the B-band and ALMA contours (see also Figure 2), for all 10 line emitters in our sample. In this appendix we discuss individual line-emitting sources in detail.

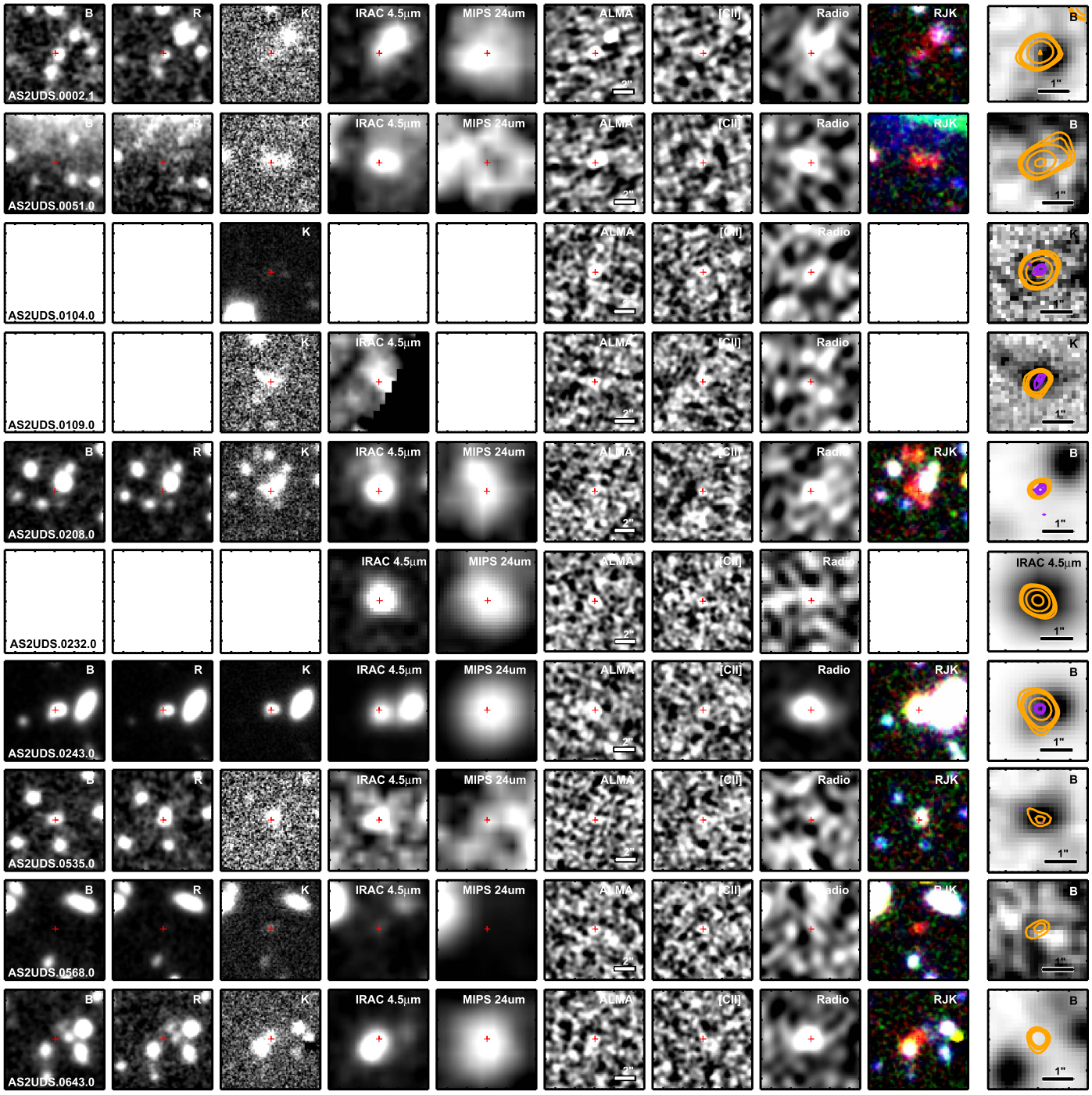

Figure 10. Multi-band thumbnails of main catalog sources. The leftmost nine thumbnails are each $10'' \times 10''$, centered on the source submillimeter emission. The red cross marks the centre of the submillimeter emission from the ALMA maps. The rightmost thumbnail is a zoomed-in $3'' \times 3''$ thumbnail with ALMA contours overlaid at 3, 4, 5, 10, and 20σ. The purple contours are high-resolution ALMA continuum emission ($\sim 0\farcs15$), where it is available, and the orange contours are at the tapered $0\farcs5$ resolution 870 μm emission.

AS2UDS.0002.1 has a *B*-band detection within $1''$ of the 870 μm emission, contaminating the photometry of the red component associated with the SMG. There is no *B*-band or radio emission at the position of the SMG, suggesting that the line we detect is likely to be [C II] at $z \sim 4.5$. However, this source may well be modestly lensed by the foreground galaxy.

AS2UDS.0051.0 has been confirmed with independent observations presented and discussed in detail in Gullberg et al. (2018). There is no obvious optical/near-infrared counterpart in the multi-wavelength thumbnails, so the most likely line identification is [C II].

AS2UDS.0104.0 has the brightest emission line in our sample. There is no optical or *Spitzer* coverage of this field, so there is little photometric information available; however, its *K*-band photometry and 1.4 GHz limit are consistent with a $z \sim 4.5$ [C II] emitter.

AS2UDS.0109.0 is not covered by many optical or near-infrared images. It has a *K* and 4.5 μm detection; however, it is

undetected at 1.4 GHz and is therefore consistent with a $z \sim 4.5$ [C II] emitter.

AS2UDS.0208.0 lies within 1″ of a bright *B*-band source with $z_{\rm phot} = 2.5 \pm 0.2$ (O. Almaini et al., in preparation), suggesting this may be a lensed $z \sim 4.5$ [C II] emitter. The SMG itself does not have an optical counterpart, first appearing in the near-infrared and is undetected at 1.4 GHz.

AS2UDS.0232.0 has no optical or near-infrared coverage. It is bright at 4.5 μm and 24 μm and undetected at 1.4 GHz. Its properties are consistent with the detected line being [C II].

AS2UDS.0243.0, in addition to a (slightly offset) *B*-band detection, is detected at 1.4 GHz (with an offset between the ALMA and radio detections of ∼0.″25). It has an 870 μm to 1.4 GHz flux ratio consistent with a $z < 4$ source ($\log_{10}(S_{870}/S_{1.4}) \sim 0.5$). The photometric redshift derived for this source is $z = 1.58 \pm 0.05$. This suggests the line we detect is CO(8–7), giving a redshift of $z = 1.63 \pm 0.01$ with a luminosity of $L_{\rm CO} = 1.5 \times 10^8\, L_\odot$. This source is therefore consistent with a $z = 1.58$ CO(8–7) line emitter.

AS2UDS.0535.0 has a *B*-band detection aligned with the 870 μm emission. The photometric redshift derived for this source is $z = 0.80 \pm 0.03$. If the photometry corresponded to the ALMA detection then the line we detect could be CO(5–4) at $z = 0.698 \pm 0.010$ with a luminosity of $L_{\rm CO} = 2.1 \times 10^7\, L_\odot$, or CO(6–5) at $z = 1.038 \pm 0.010$ with a luminosity of $L_{\rm CO} = 5.6 \times 10^7\, L_\odot$. However, this galaxy is undetected at mid-infrared and radio wavelengths, suggesting this is not a $z < 2$ star-forming galaxy but rather a $z \sim 4.5$ [C II] emitter being lensed by a foreground galaxy. There is a secondary peak in the photometric redshift distribution at $z = 4.63$, which may be more appropriate.

AS2UDS.0568.0 has no detected optical counterpart (i.e., $B > 28.4$, $R > 27.7$) in the multi-wavelength thumbnails, suggesting this is a $z \sim 4.5$ [C II] emitter.

AS2UDS.0643.0 has a photometric redshift of $z = 4.44^{+0.62}_{-1.08}$. Albeit with large error bars, this is in agreement with the line we detect being [C II] emission at $z = 4.614 \pm 0.007$. There are multiple foreground sources with $z_{\rm phot} < 4$ within 1″–2″ of AS2UDS.0643.0, which may be lensing the background SMG. This source is most likely to be a $z \sim 4.6$ SMG.

ORCID iDs

E. A. Cooke https://orcid.org/0000-0003-3843-8393
Ian Smail https://orcid.org/0000-0003-3037-257X
A. M. Swinbank https://orcid.org/0000-0003-1192-5837
S. M. Stach https://orcid.org/0000-0003-1122-6948
Fang Xia An https://orcid.org/0000-0001-7943-0166
O. Almaini https://orcid.org/0000-0001-9328-3991
J. L. Wardlow https://orcid.org/0000-0003-2376-8971
A. W. Blain https://orcid.org/0000-0001-7489-5167
Chian-Chou Chen https://orcid.org/0000-0002-3805-0789
C. J. Conselice https://orcid.org/0000-0003-1949-7638
K. E. K. Coppin https://orcid.org/0000-0002-0729-2988
D. Farrah https://orcid.org/0000-0003-1748-2010
D. Scott https://orcid.org/0000-0002-6878-9840
J. M. Simpson https://orcid.org/0000-0002-8521-1995
P. van der Werf https://orcid.org/0000-0001-5434-5942

References

Almaini, O., Wild, V., Maltby, D. T., et al. 2017, MNRAS, 472, 1401
An, F.-X., Stach, S. M., Smail, I., et al. 2018, ApJ, in press (arXiv:1806.06859)
Aravena, M., Decarli, R., Walter, F., et al. 2016, ApJ, 833, 71
Aretxaga, I., Hughes, D. H., Chapin, E. L., et al. 2003, MNRAS, 342, 759
Asboth, V., Conley, A., Sayers, J., et al. 2016, MNRAS, 462, 1989
Barden, M., Häußler, B., Peng, C. Y., McIntosh, D. H., & Guo, Y. 2012, MNRAS, 422, 449
Barger, A. J., Wang, W.-H., Cowie, L. L., et al. 2012, ApJ, 761, 89
Barro, G., Kriek, M., Pérez-González, P. G., et al. 2017, ApJL, 851, L40
Béthermin, M., Daddi, E., Magdis, G., et al. 2015, A&A, 573, A113
Blain, A. W. 1999, MNRAS, 309, 955
Bothwell, M. S., Smail, I., Chapman, S. C., et al. 2013, MNRAS, 429, 3047
Brauher, J. R., Dale, D. A., & Helou, G. 2008, ApJS, 178, 280
Brisbin, D., Ferkinhoff, C., Nikola, T., et al. 2015, ApJ, 799, 13
Capak, P. L., Carilli, C., Jones, G., et al. 2015, Natur, 522, 455
Casey, C. M., Berta, S., Béthermin, M., et al. 2012, ApJ, 761, 140
Casey, C. M., Narayanan, D., & Cooray, A. 2014, PhR, 541, 45
Chapman, S. C., Blain, A. W., Smail, I., & Ivison, R. J. 2005, ApJ, 622, 772
Chen, C.-C., Smail, I., Swinbank, A. M., et al. 2015, ApJ, 799, 194
Cooray, A., Calanog, J., Wardlow, J. L., et al. 2014, ApJ, 790, 40
Cox, P., Krips, M., Neri, R., et al. 2011, ApJ, 740, 63
da Cunha, E., Groves, B., Walter, F., et al. 2013, ApJ, 766, 13
da Cunha, E., Walter, F., Smail, I. R., et al. 2015, ApJ, 806, 110
Dalgarno, A., & McCray, R. A. 1972, ARA&A, 10, 375
Danielson, A. L. R., Swinbank, A. M., Smail, I., et al. 2017, ApJ, 840, 78
De Breuck, C., Williams, R. J., Swinbank, M., et al. 2014, A&A, 565, A59
De Looze, I., Cormier, D., Lebouteiller, V., et al. 2014, A&A, 568, A62
Díaz-Santos, T., Armus, L., Charmandaris, V., et al. 2013, ApJ, 774, 68
Díaz-Santos, T., Armus, L., Charmandaris, V., et al. 2014, ApJL, 788, L17
Díaz-Santos, T., Assef, R. J., Blain, A. W., et al. 2016, ApJL, 816, L6
Dowell, C. D., Conley, A., Glenn, J., et al. 2014, ApJ, 780, 75
Draine, B. T., Dale, D. A., Bendo, G., et al. 2007, ApJ, 663, 866
Dunne, L., Eales, S., Edmunds, M., et al. 2000, MNRAS, 315, 115
Fahrion, K., Cormier, D., Bigiel, F., et al. 2017, A&A, 599, A9
Farrah, D., Lebouteiller, V., Spoon, H. W. W., et al. 2013, ApJ, 776, 38
Geach, J. E., Dunlop, J. S., Halpern, M., et al. 2017, MNRAS, 465, 1789
Glazebrook, K., Schreiber, C., Labbé, I., et al. 2017, Natur, 544, 71
Graciá-Carpio, J., Sturm, E., Hailey-Dunsheath, S., et al. 2011, ApJL, 728, L7
Griffin, M. J., Abergel, A., Abreu, A., et al. 2010, A&A, 518, L3
Gullberg, B., De Breuck, C., Vieira, J. D., et al. 2015, MNRAS, 449, 2883
Gullberg, B., Swinbank, A. M., Smail, I., et al. 2018, ApJ, 859, 12
Hemmati, S., Yan, L., Diaz-Santos, T., et al. 2017, ApJ, 834, 36
Herrera-Camus, R., Sturm, E., Graciá-Carpio, J., et al. 2018, ApJ, in press (arXiv:1803.04422)
Hodge, J. A., Karim, A., Smail, I., et al. 2013, ApJ, 768, 91
Hodge, J. A., Swinbank, A. M., Simpson, J. M., et al. 2016, ApJ, 833, 103
Ikarashi, S., Ivison, R. J., Caputi, K. I., et al. 2015, ApJ, 810, 133
Iono, D., Yun, M. S., Elvis, M., et al. 2006, ApJL, 645, L97
Ivison, R. J., Swinbank, A. M., Swinyard, B., et al. 2010, A&A, 518, L35
Kennicutt, R. C. J. 1998, ARA&A, 36, 189
Kimball, A. E., Lacy, M., Lonsdale, C. J., & Macquart, J. P. 2015, MNRAS, 452, 88
Lagache, G., Cousin, M., & Chatzikos, M. 2018, A&A, 609, A130
Lani, C., Almaini, O., Hartley, W. G., et al. 2013, MNRAS, 435, 207
Law, D. R., Steidel, C. C., Erb, D. K., et al. 2009, ApJ, 697, 2057
Lawrence, A., Warren, S. J., Almaini, O., et al. 2007, MNRAS, 379, 1599
Luhman, M. L., Satyapal, S., Fischer, J., et al. 2003, ApJ, 594, 758
Lutz, D., Berta, S., Contursi, A., et al. 2016, A&A, 591, A136
Madau, P., & Dickinson, M. 2014, ARA&A, 52, 415
Madden, S. C., Poglitsch, A., Geis, N., Stacey, G. J., & Townes, C. H. 1997, ApJ, 483, 200
Magnelli, B., Elbaz, D., Chary, R. R., et al. 2011, A&A, 528, 35
Magnelli, B., Lutz, D., Santini, P., et al. 2012a, A&A, 539, A155
Magnelli, B., Saintonge, A., Lutz, D., et al. 2012b, A&A, 548, A22
Maiolino, R., Nagao, T., Grazian, A., et al. 2008, A&A, 488, 463
Malhotra, S., Kaufman, M. J., Hollenbach, D., et al. 2001, ApJ, 561, 766
McMullin, J. P., Waters, B., Schiebel, D., Young, W., & Golap, K. 2007, in ASP Conf. Ser. 376, Astronomical Data Analysis Software and Systems XVI, ed. R. A. Shaw, F. Hill, & D. J. Bell, 127
Michałowski, M. J., Dunlop, J. S., Koprowski, M. P., et al. 2017, MNRAS, 469, 492
Miller, T. B., Chapman, S. C., Hayward, C. C., et al. 2016, MNRAS, submitted (arXiv:1611.08552)
Oliver, S. J., Bock, J., Altieri, B., et al. 2012, MNRAS, 424, 1614
Peacock, J. A., Rowan-Robinson, M., Blain, A. W., et al. 2000, MNRAS, 318, 535
Peng, C. Y., Ho, L. C., Impey, C. D., & Rix, H.-W. 2002, AJ, 124, 266

Pineda, J. L., Langer, W. D., Velusamy, T., & Goldsmith, P. F. 2013, A&A, 554, A103
Poglitsch, A., Waelkens, C., Geis, N., et al. 2010, A&A, 518, L2
Popping, G., Caputi, K. I., Trager, S. C., et al. 2015, MNRAS, 454, 2258
Popping, G., van Kampen, E., Decarli, R., et al. 2016, MNRAS, 461, 93
Rangwala, N., Maloney, P. R., Glenn, J., et al. 2011, ApJ, 743, 94
Riechers, D. A., Bradford, C. M., Clements, D. L., et al. 2013, Natur, 496, 329
Roseboom, I. G., Ivison, R. J., Greve, T. R., et al. 2012, MNRAS, 419, 2758
Salpeter, E. E. 1955, ApJ, 121, 161
Santini, P., Maiolino, R., Magnelli, B., et al. 2010, A&A, 518, L154
Sargsyan, L., Lebouteiller, V., Weedman, D., et al. 2012, ApJ, 755, 171
Schreiber, C., Elbaz, D., Pannella, M., et al. 2018, A&A, 609, A30
Schreiber, C., Pannella, M., Leiton, R., et al. 2017, A&A, 599, 134
Simpson, J. M., Smail, I., Swinbank, A. M., et al. 2015, ApJ, 799, 81
Simpson, J. M., Smail, I., Swinbank, A. M., et al. 2017a, ApJ, 839, 58
Simpson, J. M., Smail, I., Wang, W.-H., et al. 2017b, ApJL, 844, L10
Simpson, J. M., Swinbank, A. M., Smail, I., et al. 2014, ApJ, 788, 125
Smail, I., Ivison, R. J., & Blain, A. W. 1997, ApJL, 490, L5
Smail, I., Swinbank, A. M., Ivison, R. J., & Ibar, E. 2011, MNRAS, 414, L95
Smith, J. D. T., Croxall, K., Draine, B., et al. 2017, ApJ, 834, 5
Stacey, G. J., Geis, N., Genzel, R., et al. 1991, ApJ, 373, 423
Stacey, G. J., Hailey-Dunsheath, S., Ferkinhoff, C., et al. 2010, ApJ, 724, 957
Swinbank, A. M., Karim, A., Smail, I., et al. 2012, MNRAS, 427, 1066
Swinbank, A. M., Simpson, J. M., Smail, I., et al. 2014, MNRAS, 438, 1267
Swinbank, A. M., Smail, I., Chapman, S. C., et al. 2010b, MNRAS, 405, 234
Swinbank, A. M., Smail, I., Longmore, S., et al. 2010a, Natur, 464, 733
Symeonidis, M., Vaccari, M., Berta, S., et al. 2013, MNRAS, 431, 2317
Tacconi, L. J., Genzel, R., Saintonge, A., et al. 2018, ApJ, 853, 179
Toft, S., Smolčić, V., Magnelli, B., et al. 2014, ApJ, 782, 68
van der Werf, P. P., Isaak, K. G., Meijerink, R., et al. 2010, A&A, 518, L42
Venemans, B. P., McMahon, R. G., Walter, F., et al. 2012, ApJL, 751, L25
Venemans, B. P., Walter, F., Zschaechner, L., et al. 2016, ApJ, 816, 37
Walter, F., Decarli, R., Carilli, C., et al. 2012, ApJ, 752, 93
Wang, R., Wagg, J., Carilli, C. L., et al. 2013, ApJ, 773, 44
Wardlow, J. L., Smail, I., Coppin, K. E. K., et al. 2011, MNRAS, 415, 1479
Willott, C. J., Carilli, C. L., Wagg, J., & Wang, R. 2015, ApJ, 807, 180
Yang, C., Omont, A., Beelen, A., et al. 2017, A&A, 608, A144
Yuan, F., Buat, V., Burgarella, D., et al. 2015, A&A, 582, A90
Yun, M. S., Scott, K. S., Guo, Y., et al. 2012, MNRAS, 420, 957
Zavala, J. A., Aretxaga, I., Geach, J. E., et al. 2017, MNRAS, 464, 3369